VIII. APPLIED PLASMA RESEARCH*

A. Active Plasma Systems

Academic and Research Staff

Prof. L. D. Smullin	Prof. R. R. Parker
Prof. R. J. Briggs	Prof. K. I. Thomassen

Graduate Students

Y. Ayasli	J. A. Mangano	J. A. Rome
R. K. Linford	P. J. McCleer	J. M. Tarrh, III
	M. I. Mirkin	

1. DUAL-BEAM PLASMA SOURCE

Introduction

This is a report of the major design considerations for a new plasma source. The source is to produce a steady, warm, highly ionized, moderately dense, hydrogen plasma. This plasma will enable us to study a variety of low-frequency instabilities.

At present, Q-machines and Lisitano structures come closer to producing the desired plasma than do other sources. The major limitation of the Q-machine plasma is that the effects of electron and ion temperatures on the low-frequency phenomena cannot be studied because the temperatures are very low and the ions are massive. The plasma produced by a Lisitano structure is very sensitive to the magnetic field. Thus it is very difficult to investigate the effect of the magnetic field on a plasma instability. A commonly observed limitation of the Lisitano structure is that the plasma density is so limited that the electron plasma frequency is less than or equal to the electron-cyclotron frequency. The new source should eliminate all of the mentioned deficiencies.

The expected maximum plasma parameters of the new source include: density, 10^{12} cm^{-3}; $T_e \approx 15$ eV; and $T_i \approx 1$ eV. The neutral gas pressure will be approximately 10^{-5} Torr to yield an ionization of approximately 70%. The maximum magnetic field available is 3 kG.

The discussion of the plasma system is divided into two main parts: the plasma source, and the plasma confinement region. In most plasma sources, the region of plasma generation is not suitable for studying low-frequency instabilities, wave-wave interaction, and so forth, because of the low percentage of ionization and generally turbulent nature of the plasma in this region. Therefore the "source" and the region

---

*This work is supported by the National Science Foundation (Grant GK-18185).

where the plasma is studied must be considered two separate parts of the system.

The plasma source that has been chosen is a beam-plasma discharge (BPD) which can produce a dense, warm plasma without the sensitivity to magnetic field exhibited by the Lisitano structure.

The confinement region has been designed to achieve two objectives. First, the plasma coming from the source must be differentially pumped to achieve low neutral pressure. Second, the system is made longitudinally symmetrical to eliminate the rapid drift of the hydrogen plasma inside the confinement region.

Regardless of the method of plasma production in an open-ended system, the plasma tends to drift out of the system at about half the ion sound speed; that is, $v_d \approx \sqrt{kTe/m_i}$. For the projected parameters of the system, the transit time of the hydrogen plasma through a 1-m drift tube is approximately 20 μs. Since this transit time is comparable to or less than the characteristic times of important low-frequency instabilities, the drift seriously affects their behavior. This drift should be greatly reduced in the confinement region by making it symmetrical. The effect of this drift is not as severe in argon or alkali-metal plasmas, because of the larger ion mass.

Source

The plasma source (Fig. VIII-1) comprises an electron-gun assembly, a plasma generation chamber, and an electron-beam collector. The inverted, magnetron-injection gun emits a hollow cylindrical beam, 2.5 cm in diameter and 1 mm thick, into the generation chamber where it interacts with the injected hydrogen gas. The hollow beam is stopped by the beam collector to allow the central core of plasma

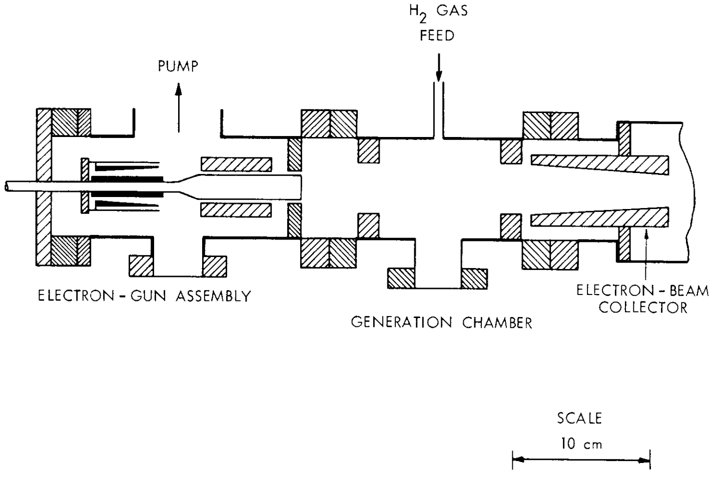

Fig. VIII-1. Plasma source.

to stream through the hole in the annular collector.

An initial test of the plasma source has been made, using a standard magnetron injection gun like the one described by Mangano and Smullin in Section VIII-A. 2. The test was successful in generating a plasma with $n = 10^{11}$ and $T_e = 15$ eV. The density was limited by the severe but expected thermal load on the cathode.

The electron gun shown in Fig. VIII-2 has several advantages as a plasma source over the standard magnetron gun. The major source of heat, which limits the standard gun, came from bombardment of the cathode by plasma ions. The ion collector in the gun assembly is designed to pull the ions out of the plasma before they can reach the cathode. There are three basic advantages with this arrangement:

1. The energy is deposited on the ion collector which can be easily water-cooled.
2. Less power is wasted, since the potential on the ion collector need not be as large as the cathode.
3. The cathode and its power supply are isolated from the plasma, thereby permitting entirely independent control of the electron-beam parameters.

Two additional advantages have been built into the gun assembly. The anode in

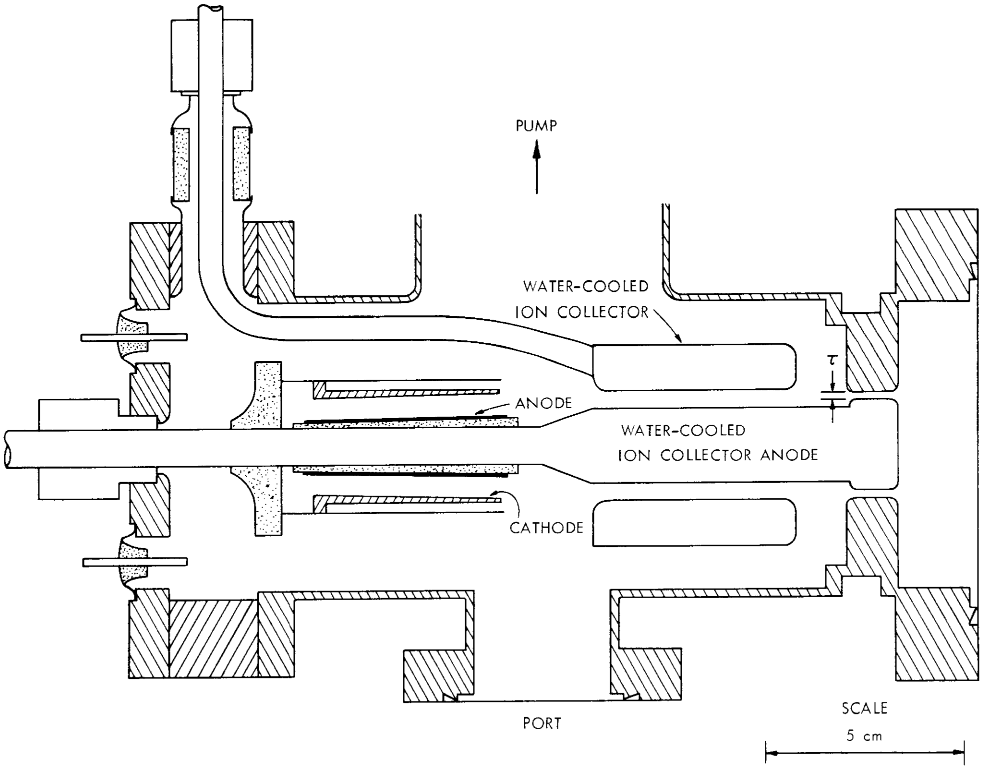

Fig. VIII-2. Electron-gun assembly.

the electron gun can be biased to give independent control of beam energy and perveance. The ion collector anode can be biased slightly negative so that the end of the rod acts as a planar probe biased in the ion saturation region. Therefore, if the electron temperature is known, the plasma density can be easily determined. Also, when the ion collector anode is biased in the ion saturation region, it should improve the radial uniformity of the plasma by reflecting electrons and hence decreasing axial plasma losses in the neutral-core region.

For the ion collector to work effectively, four criteria must be met. First, the radial electric field in the gap between the ion collector and its anode must be large enough to establish an ion Larmor radius larger than the thickness, τ, of the plasma shell. In terms of the voltage, V_i, on the ion collector, this condition is satisfied in the absence of plasma if $V_i > 2B^2\tau^2$, where B is in kG, τ in mm, and V_i in volts.

The second condition is that the electric field must be capable of penetrating the plasma in the gap between the ion collector and its anode. This condition can exist if the Debye length of the plasma is greater than τ (which is generally not the case), or if the electric field is large enough to deplete the ions from the gap as rapidly as the plasma can supply them, and thus not allow a plasma to exist in the gap. This condition can be compared with a cathode in temperature-limited flow. The plasma in the generation chamber acts as an ion emitter capable of supplying a current density J_m, which is dependent on the density and electron temperature of the plasma. If the voltage on the ion collector exceeds the value V_m, which is related to J_m by the Child-Langmuir law for space charge-limited flow, "temperature-limited" flow is achieved. For this condition in planar geometry significant space charge cannot exist and thus plasma cannot exist in the gap. Because of the cross-field geometry of the system, a plasma can exist in the gap near the generation chamber end of the ion collector, but the plasma must be completely depleted at the cathode end. This calculation results in the following condition:

$$V_i > 250\,\tau^2\left(\frac{n}{\ell}\right)^{2/3}\left(\frac{kTe}{e}\right)^{1/3}.$$

The plasma density n is in units of 10^{12} cm^{-3}, τ in mm and the length of the ion collector ℓ in cm. For the plasma parameters under consideration this second constraint on the ion collector voltage is the dominant condition. It is now apparent why the gap thickness τ is kept as small as possible.

The third constraint is that the beam electrons should not be deflected into the ion collector anode by the electric field. This establishes the following upper bound on the voltage V_i:

$$V_i < 10^3\,B^2\tau^2.$$

The fourth and last constraint on the ion collector is that it must be capable of dissipating the energy deposited by the ions. The power in kW is given by

$$P = 5 \times 10^{-4}\, n\tau D\left(\frac{kTe}{e}\right)^{1/2} V_i > 0.12\, \tau^3 n^{5/3} \frac{D}{\ell^{2/3}} \left(\frac{kTe}{e}\right)^{5/6},$$

where the inside diameter, D, of the ion collector is in cm. Because of the strong dependence of P on τ and n, a safety factor of at least 10 should be included. For the maximum plasma parameters, this requires the anode to handle approximately 20 kW of power. By machining special finned water channels in the ion collector, this can be accomplished with standard water-line pressures of 40 psi.

Constraints imposed by electrical connections and water cooling forced us to adopt the present inverted cathode design. As can be seen from Fig. VIII-2, the electrons are emitted radially inward from the cathode surface as opposed to the usual magnetron-injection gun.

The pumping port in the gun assembly maintains a lower gas pressure in this region than in the plasma-generation chamber. This prevents significant plasma generation in the gun assembly.

The main design consideration of the plasma-generation chamber is its length. Data obtained by Mangano and Smullin show that the major beam-plasma microwave interaction occurs within 25 cm of the gun. Thus making the plasma generation chamber longer than ~25 cm would serve no purpose.

The electron-beam collector is tapered to increase the impact area of the electron beam, thereby reducing the local heating. It is water-cooled in the same manner as the ion collector and can handle a 5 kW beam with a safety factor of 8.

Confinement Region

The entire system including the confinement region is shown in Fig. VIII-3. The system is symmetrical and requires two identical plasma sources. The differential pumping regions are designed to maintain a factor of 15 difference in pressure between the generation chambers and the drift region without a plasma. The plasma will decrease the flow of neutral gas into the drift region, but recombination on the walls of that region may offset the decreased flow. For a neutral pressure of 2×10^{-4} Torr in the generation region, a neutral pressure of the order of 10^{-5} Torr is expected in the drift region.

The system is symmetrical to reduce the drift of the plasma in the confinement region. If radial losses are ignored, the axial drift in this region should be zero. This can be explained by examining the self-consistent solution of the zero-order potential, density, generation rate, and loss rate of the plasma. The work done by

Dunn and Self[1] has been extended by Linford.[2]

The results indicate that in a region of plasma generation, the potential is larger than it is near the axial boundaries of the plasma by $\alpha \frac{kTe}{e}$, where $\alpha \approx 1$. In a region where there is no plasma generation, but is bounded on one end by a plasma-generation region and on the other by a sheath and a wall, the potential is axially uniform and $\alpha \frac{kTe}{e}$ is less than in the generation region. The potential drop between the generation region and the drift region provide the ions with the well-known drift $v_D \sim \sqrt{kTe/m_i}$. This drift given to the ions is necessary to satisfy the Langmuir sheath criterion[3] at the wall boundary, that is, to preserve ambipolar loss. If, however, the drift region is bounded on both ends by symmetrical plasma generation regions, and if radial losses are ignored, then no net loss from this region occurs in the steady state. Under these conditions, it can be shown that the potential in this central region is the same as in the generation regions and hence no drift occurs.

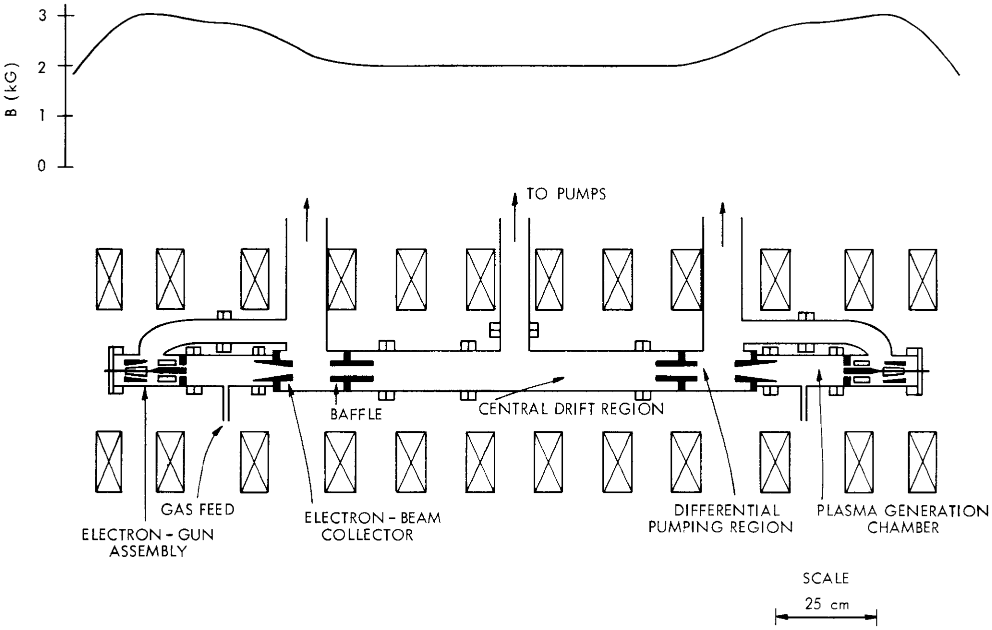

Fig. VIII-3. Symmetrical plasma system.

The radial loss in the drift region will be much smaller than the axial loss from an unsymmetrical, one-source system, but the loss will not be zero. The expected result of finite radial loss is a slight potential depression in the drift region, which results in two slowly contrastreaming plasmas. The magnitude of this drift has not been calculated because the radial loss rate is not known.

One potential problem with this method of decreasing the axial drift, is that the plasma-generation rate in one source is not entirely independent of the other source. This coupling between the two sources through the plasma electrons can lead to a "generation" instability. Some stabilizing mechanism will probably be needed to avoid this problem. The most likely approach is to control the beam power with a simple feedback system.

The plasma system is being assembled at the present time.

R. K. Linford, L. D. Smullin

References

1. D. A. Dunn and S. A. Self, "Static Theory of Density and Potential Distribution in a Beam-Generated Plasma," J. Appl. Phys. 35, 113 (1964).
2. R. K. Linford, "Ion Energy Analysis in a Beam-Plasma Discharge," S. M. and E. E. Thesis, Department of Electrical Engineering, M. I. T. , 1969.
3. G. Suits (ed.), Collected Works of Irving Langmuir, Vol. 5 (Macmillan Company, New York, 1961).

2. MICROWAVE INSTABILITIES IN A BEAM-PLASMA DISCHARGE

Introduction

In this report, we shall present experimental data obtained recently in our study of the beam-plasma discharge (BPD). Detailed measurements of the microwave frequency spectrum of the self-generated oscillations have been made and correlated with the interaction between the negative energy, slow space-charge wave supported by the electron beam and the electron plasma wave. In an axially uniform, static magnetic field, this intense microwave interaction has been found to grow exponentially, saturate, and decay in an axial region of approximately 15 cm directly in front of the electron gun. This axial profile of RF amplitude exists, although the plasma column is 70 cm long. Measurements of the beam and plasma densities, plasma electron temperature, wave number spectrum, and axial growth rates for the interaction are also given. We hope that these data, together with data to be obtained, will lead to a coherent, quantitative understanding of the microscopic processes involved in sustaining and heating the BPD.

Description of the Experimental Apparatus

Figure VIII-4 is a schematic diagram of the experimental apparatus (system C)[1], including the orientation of the four probes used in making the measurements to be described here. Those labeled P_1 and P_2 are axially movable and, together with a motor drive, were used primarily in making RF measurements. The probe labeled

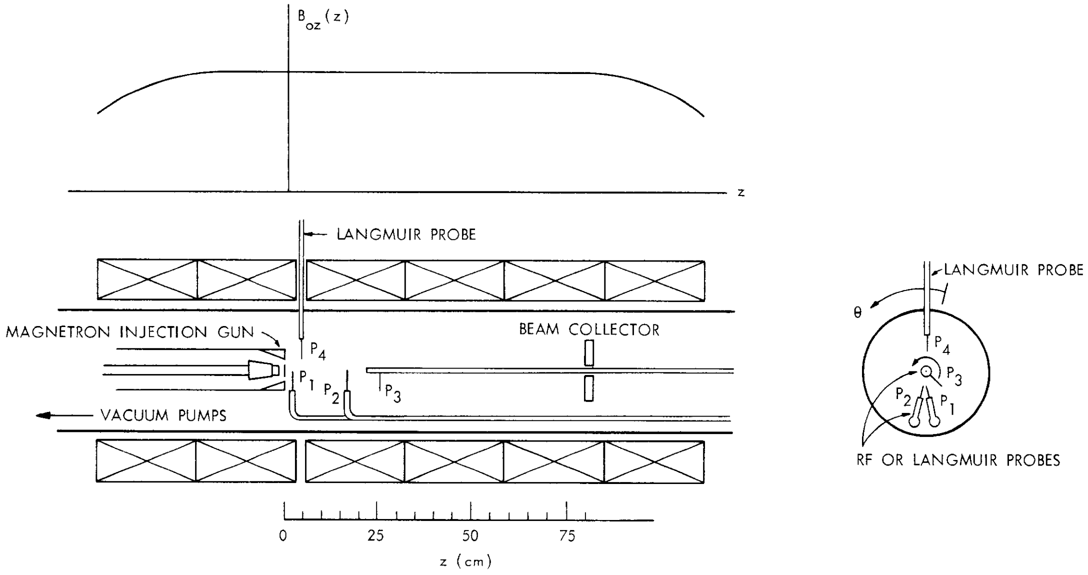

(a) (b)

Fig. VIII-4. (a) Beam-Plasma Discharge apparatus.
(b) Gun view of the RF and Langmuir probes.

P_3 is movable axially or azimuthally, with a motor drive. The fourth probe, P_4, was moved radially with a micrometer head drive to determine Langmuir probe characteristics as a function of radius. All of these probes were constructed from semirigid coaxial line (0.141 in. O.D.) with 0.015 in. holes drilled in the center conductors to accommodate 0.015 in. O.D. tungsten wire extensions of the center conductor. An outer jacket of 0.25 in. O.D. (0.030 wall) stainless-steel tubing was used on each probe to improve the rigidity of the probe structure. Since the teflon insulation used in the coaxial line provided a vacuum seal between inner and outer

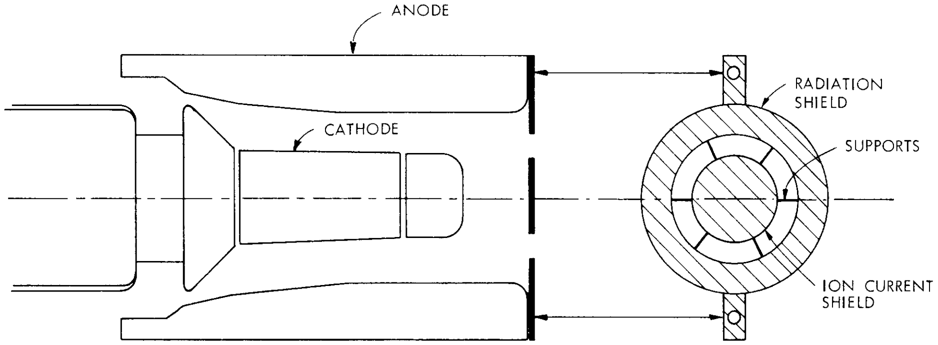

Fig. VIII-5. Magnetron injection gun structure.

conductors, this probe construction technique insured a low VSWR, as seen from the probe tip looking back through to the signal-processing equipment.

In the experiments described here, the magnet system was used to produce a uniform axial magnetic field of between 800 G and 1200 G over the entire length of the discharge region. The vacuum system, which has been described elsewhere,[1] produced a base pressure of ~5 × 10^{-7} Torr. During system operation the discharge chamber was filled with hydrogen gas to pressures of between 0.5 Torr and 1.0×10^{-3} Torr.

The magnetron injection gun, shown in Figs. VIII-4 and VIII-5, is composed of an oxide-coated nickel cathode, a copper anode, and two shields with supports. The ion current shield prevents plasma ions from drifting back into the cathode structure and loading down the voltage supply for the gun. This shield is a molybdenum disk, 3 mil thick, supported by thick molybdenum vanes, 3 mil thick and 0.15 in. wide. The radiation shield is used to prevent some of the radiation emitted from the cathode from heating the probes. The gun produces a hollow electron beam (r ~ 1.15 cm and t = 1 mm), with a perveance ~8 μperv in vacuum. The electron gun is normally pulsed on for a period of 700 μs at a repetition rate varying from 1 to 5 pulses per second. The cathode voltage is variable up to 10 kV.

Figure VIII-6 shows the angular distribution of beam current coming from the

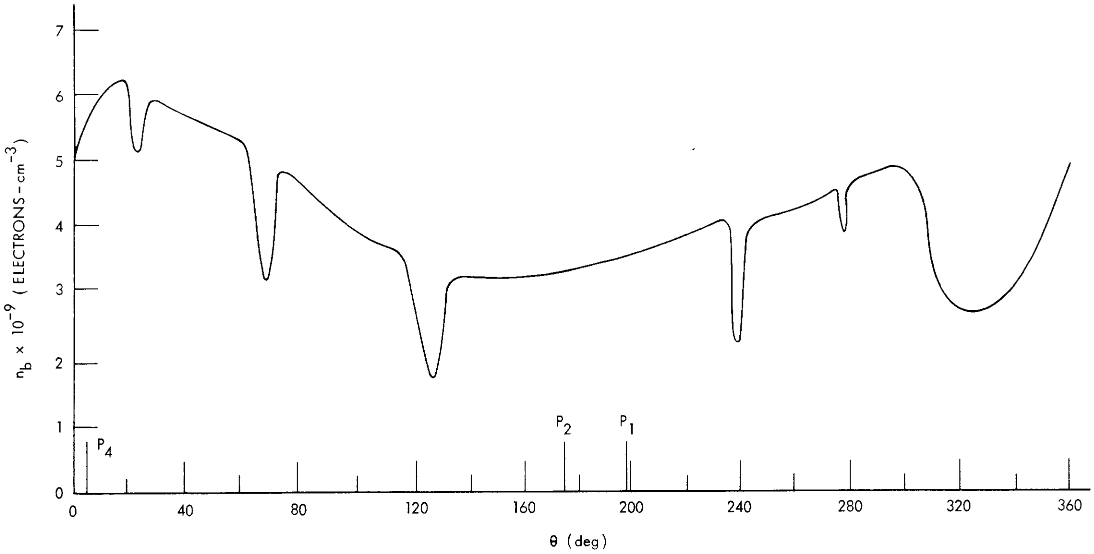

Fig. VIII-6. Electron beam current vs azimuth. Operating conditions:

$V_k = 4.6$ kV $\quad B_o = 940$ G

$I_k = 2.5$ A $\quad P_o = 5 \times 10^{-7}$ Torr.

electron gun at an axial position 5 cm from the ion current collector. This curve was obtained by rotating probe P_3 azimuthally and recording the voltage developed across a 50 Ω resistor at the probe output. The six dips in the current at various θ are caused by the six vanes supporting the ion current collector. One of these supports (at θ ~ 320°) is twisted, thereby resulting in the broader dip seen at its angle. The positions of probes P_1, P_2, and P_4 are also shown in Fig. VIII-6.

Plasma Density and Electron Temperature Measurements

The radial profiles of the time-averaged electron density and temperature have been measured as a function of radius and are plotted in Fig. VIII-7. These measurements were made with probe P_4 at the axial position z = 5 cm. As seen from the data, the plasma column is annular in cross section and is confined to within a few millimeters of the annular electron gun. The electron temperature, however, appears to peak twice at radii just inside and outside the plasma annulus and to decrease monotonically outside these peaks.

An interesting explanation for the measured transverse profile of the electron temperature can be hypothesized. Because the plasma column is radially inhomogeneous, the cold-plasma, long-wavelength mode excited in the beam region can couple

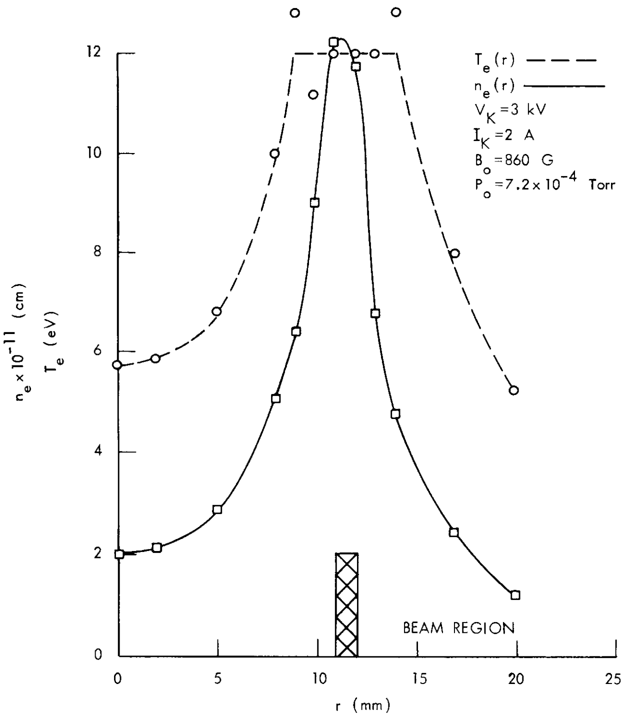

Fig. VIII-7. Electron temperature and density vs radius.

to the hot plasma, short-wavelength, Bernstein-like mode at radii where the frequency is equal to the local upper hybrid frequency.[2-6] This short wavelength mode is rapidly damped with its wave energy being converted to random electron energy (that is, electron temperature). This picture would predict increased electron temperature in regions just inside and outside the electron beam annulus where the coupling occurs. This prediction is consistent with and may possibly be connected with the apparent increase in electron temperature at radii just outside the peak in the radial density profile.

The electron temperature and density profiles shown here were measured at an axial position well before the beam-plasma interaction had grown to its saturated value. Thus far it has not been possible to measure this profile as a function of z because a probe movable in both radial and axial directions has not been built. We are now building such a probe, however. The data from this probe should indicate whether (i) the plasma annulus increases in thickness, which would result in a decrease in $k_\perp$, (ii) the peak plasma density varies significantly in z; and (iii) the peaks in electron temperature at radii adjacent to the plasma annulus are accentuated at axial positions where the beam-plasma interaction amplitude is large.

Frequency Spectrum Measurements for $f_{pe} > f_{ce}$

The time-averaged frequency spectrum of microwave power emitted from our BPD is plotted in Fig. VIII-8 for one set of operating conditions. Eventually we shall show that the oscillations are self-generated by the interaction between the slow space-charge wave of the electron beam interacting with the propagating plasma wave near f_{pe}. The wideband nature of the spectrum sample shown in this figure is due to fluctuations (in time) of the electron plasma density, and consequently of the electron plasma frequency (f_{pe}) during the many successive RF pulses in the averaging period.[7]

Figure VIII-9 shows plots of the plasma density and electron temperature as a function of the instantaneous frequency of the self-generated oscillations. These data were obtained by measuring the Langmuir probe characteristic during the most intense bursts of radio frequency at a given frequency. Langmuir-probe curves were thus obtained as a function of the instantaneous frequency. The data shown in Fig. VIII-9 were then extracted from these Langmuir-probe curves. From these data we conclude that the instantaneous frequency of the self-generated oscillations is approximately given by the instantaneous value of the electron plasma frequency adjacent to the beam region if $f_{pe} > f_{ce}$ and $f_{pe} \neq f_{ce}, 2f_{ce}$.

The measured spectra in the frequency regime $f > f_{ce}$ are also characterized by minima at frequencies $f = nf_{ce}$, where $n = 1, 2, 3$. The frequency of these minima

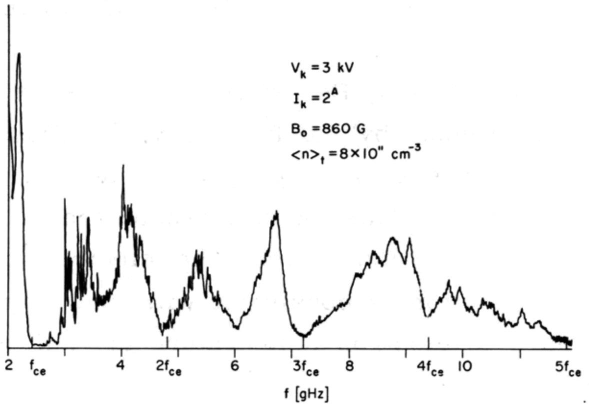

Fig. VIII-8. Time-averaged frequency spectrum of microwave oscillations. Electron cyclotron harmonics are shown.

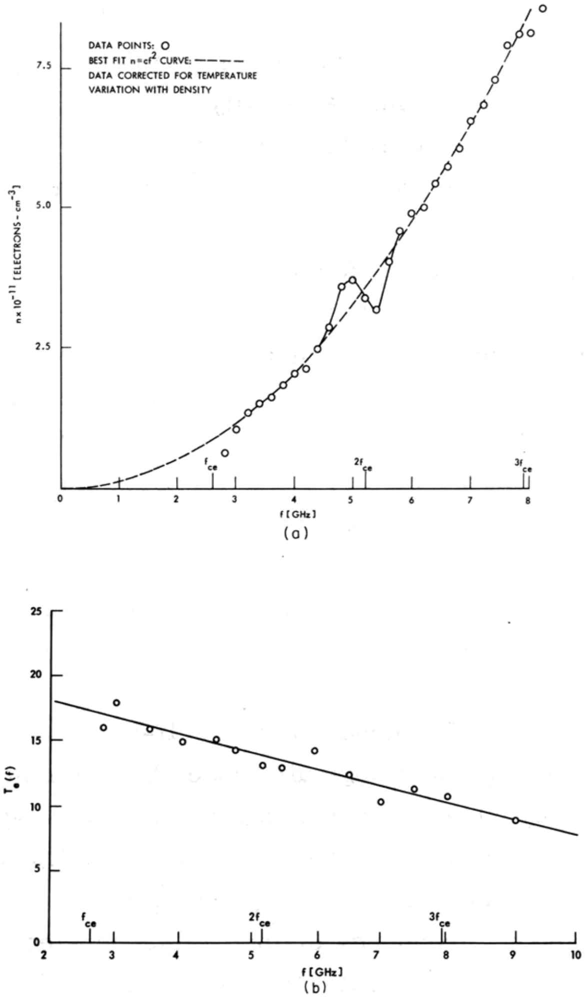

Fig. VIII-9. (a) Electron density as a function of frequency.
(b) Electron temperature as a function of frequency.

are plotted in Fig. VIII-10 as a function of the measured, static magnetic field, B_o. The equations of the lines drawn through the plotted points are given by $f_n = neB_o/m_e$, where $n = 1, 2, 3$. These minima are interpreted as being caused by electrostatic electron-cyclotron damping of the primary beam-plasma interaction when the instantaneous frequency ($\sim f_{pe}$) is near nf_{ce}. The detailed structure of the frequency spectrum in regions between the electron-cyclotron harmonics is strongly dependent on the axial position of the probe used to measure the spectrum. In fact, the minima in the frequency spectrum shown in Fig. VIII-8 may be explained by the different axial growth, saturation, and decay profiles of the RF amplitude at different frequencies. We shall show that the growth rate for the interaction is minimum near cyclotron harmonics and maximum between. Therefore the relative minima between cyclotron harmonics observed in Fig. VIII-8 may mean that the oscillation amplitude has grown and already decayed at these frequencies and position.

Wave-number Measurements for $f_{pe} > f_{ce}$

Figure VIII-11 illustrates a typical curve of RF intensity at a given frequency ($f > f_{ce}$) vs axial distance. It shows the exponential growth out of noise, saturation, and rapid decay within a relatively short distance. Curves like Fig. VIII-11 were taken at frequencies over the range covered by Fig. VIII-9, and the exponential growth rates were determined (before saturation). Figure VIII-12 shows what we interpret as Im ($k_{\parallel}$) as a function of frequency. The pattern of growth from a noise level at $z = 0$ to saturation clearly indicates a convective instability. This result, in turn, implies that the electron plasma wave with which the slow space-charge wave on the beam interacts is a forward wave at the point of synchronism. Figure VIII-12 also illustrates the effects of electrostatic electron-cyclotron damping of the beam-plasma interaction at harmonics of the electron cyclotron frequency.[8]

Figure VIII-13 is a plot of the measured real part of the wave number; $k_{\parallel_r}$, against frequency. Also shown in this figure is the wave number vs frequency characteristic of the slow space-charge electron beam wave (dashed line), with the space-charge reduction factor neglected. The proper electron beam-plasma frequency (f_{pb}) was determined from our measurement of the electron beam density (Fig. VIII-6) in the region near probes P_1 and P_2. Figure VIII-12 illustrates clearly that the interaction of the plasma with the beam is through the slow space-charge wave of the beam, and not the slow cyclotron wave.

Figure VIII-14 is a chart recording of an interferogram produced by the balanced mixing of signals from a fixed and an axially moving probe (probes labelled P_1 and P_2). Such curves were used to produce Fig. VIII-13. In our first attempts, we were unable to detect any such interference pattern. We finally discovered that the two

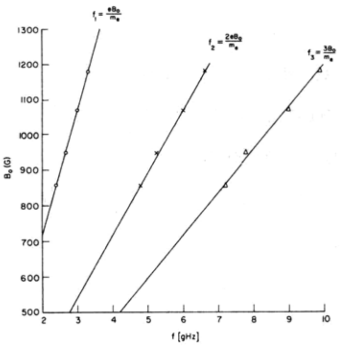

Fig. VIII-10.

Measured magnetic field plotted against the frequency of the minima in the measured frequency spectra for 3 different axial magnetic field amplitudes.

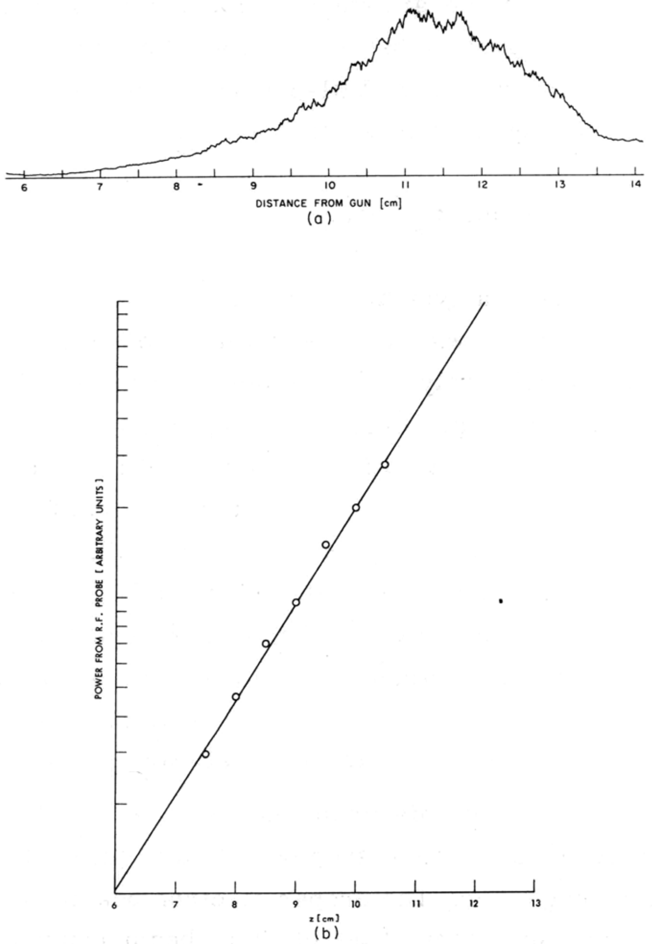

Fig. VIII-11. (a) Relative power in oscillations at f = 3.85 GHz vs axial distance from the electron gun.

(b) Relative power in oscillations at f = 3.85 GHz before axial saturation vs axial distance from the electron gun. Operating conditions:

$V_k = 4.6$ kV $\quad B_o = 940$ G

$I_k = 3.6$ A $\quad P_o = 7.2 \times 10^{-4}$ Torr.

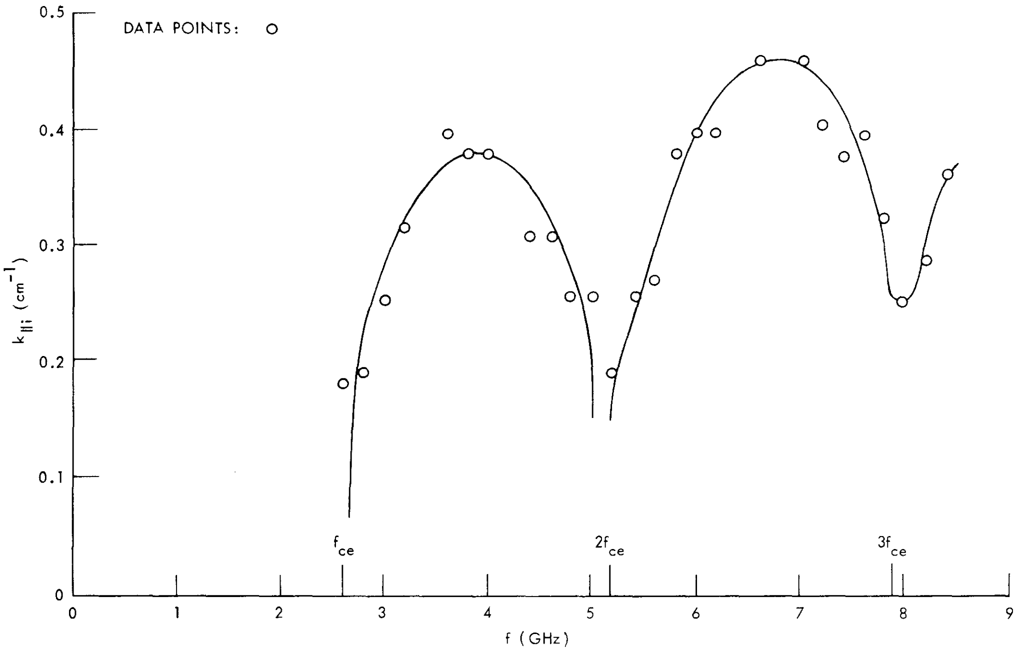

Fig. VIII-12. Imaginary part of the axial wave number vs frequency. Operating conditions are the same as for Fig. VIII-11.

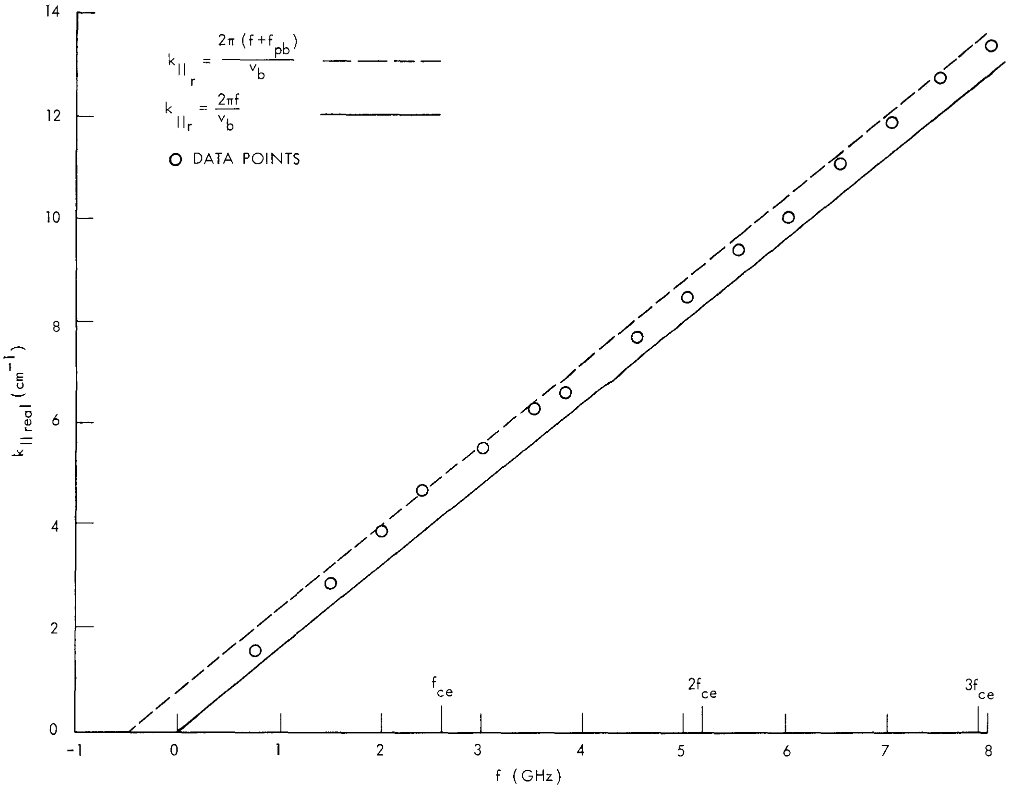

Fig. VIII-13. Real part of the axial wave number vs frequency. Operating conditions are the same as for Fig. VIII-11.

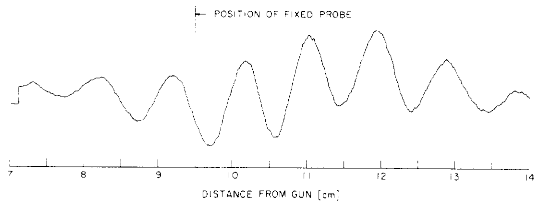

Fig. VIII-14. Interference pattern between probe P_1 fixed at z = 9 cm and probe P_2 plotted against the distance of the probe P_2 from the electron gun. Operating conditions are the same as for Fig. VIII-11.

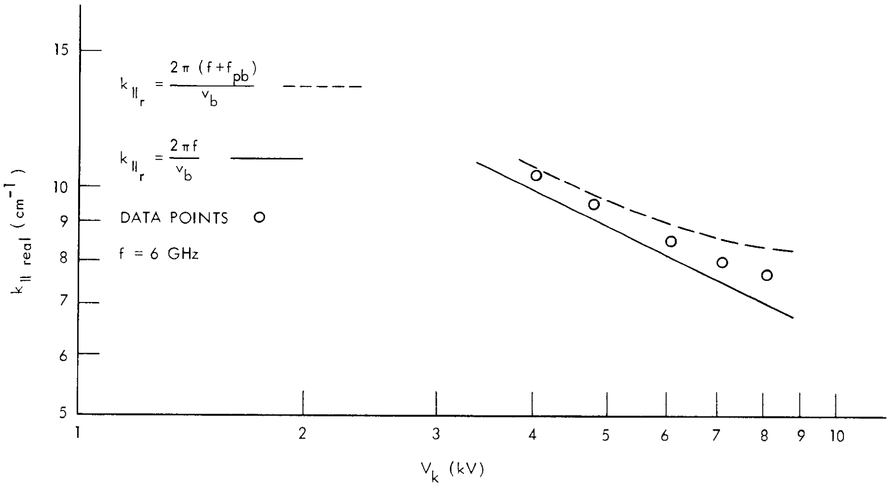

Fig. VIII-15. Real part of the axial wave number vs beam voltage. Operating conditions: B_o = 940 Gauss; P_o = 7.2 × 10^{-4} Torr.

probes must be at very nearly the same azimuthal position in the cross section in order to have coherent signals.

Finally, Fig. VIII-15 is a plot of $k_{\|_r}$ against V_k, the gun cathode voltage, at a fixed frequency of 6 GHz. Also shown in this figure is a plot of the relationship between Re ($k_{\|}$) and V_k for the slow space-charge wave on the electron beam (dashed line). Again the proper electron beam plasma frequency (f_{pb}) was determined from our measurement of the electron-beam density (as in Fig. VIII-6) in the region near probes P_1 and P_2. The slight bow in these curves is caused by the increase in f_{pb} with the cathode voltage $\left(f_{pb} \alpha V_k^{1/2}\right)$. Figure VIII-15 shows that the interaction of the plasma with the beam is through the slow space-charge wave of the beam at V_k from 4 kV to 8 kV in our discharge.

J. A. Mangano, L. D. Smullin

References

1. J. A. Mangano, "Excitation of Ion Cyclotron Waves in a Beam-Generated Plasma," S. M. Thesis, Department of Electrical Engineering, M. I. T. , 1968.
2. R. J. Briggs and S. F. Paik, Int. J. Electronics 23, 163 (1968).
3. L. D. Pearlstein and D. K. Bhadra, Phys. Fluids 12, 213 (1969).
4. S. J. Buchsbaum and A. Hasegawa, Phys. Rev. 143, 303 (1966).
5. D. E. Baldwin, J. Plasma Phys. 1, 289 (1967).
6. V. Kopecky, et al. , J. Plasma Phys. 3, 179 (1969).
7. M. Seidl and P. Sunka, Nucl. Fusion 7, 237 (1967).

3. STABILITY THEOREMS FOR AN ELECTRON BEAM WITH VELOCITY SHEAR IN A LARGE LONGITUDINAL MAGNETIC FIELD

In previous reports,[1,2] we have considered the stability of a cold electron beam in an infinite longitudinal magnetic field. We have now generalized this to the case of a cylindrical electron beam focused by a large $\left(\omega_c^2 \gg \omega_p^2\right)$ DC magnetic field, $\bar{B}_0$. In general, the equilibrium electron velocity and density are functions of the radius, r. We consider equilibria for which the beam is unrippled, so that v_{0z} and $v_{0\theta} \equiv \Omega r$ are the only nonzero components of the velocity. This geometry is illustrated in Fig. VIII-16.

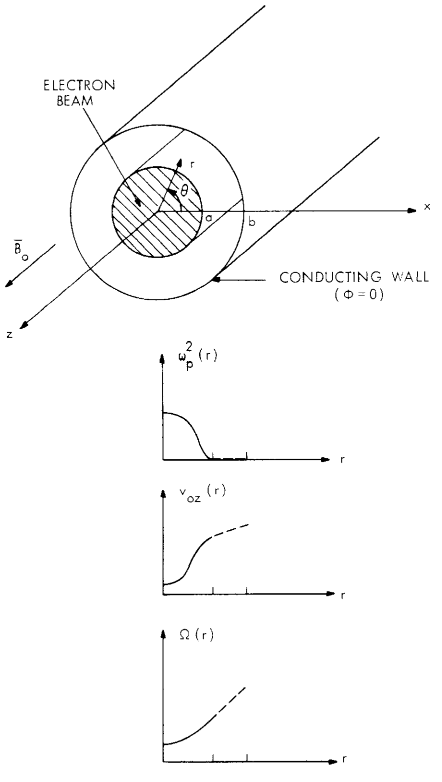

Fig. VIII-16.
Geometry of the problem.

Because ω_c is large, the small-signal perpendicular velocity is approximately $v_{1\perp} \approx (\bar{E}_1 \times \bar{B}_0)/B_0^2$. Under this assumption, the equation obeyed by the small-signal potential can be easily derived.[3]

$$\frac{d^2\phi}{dr^2} + \frac{1}{r}\frac{d\phi}{dr} + \phi\left\{-\frac{\ell^2}{r^2} - k^2 + \frac{k^2\omega_p^2}{\omega_d^2}\left[1 - \frac{\ell v_{0z}'}{kr\omega_c}\right] - \frac{\ell}{r}\frac{\left(\omega_p^2\right)'}{\omega_c\omega_d}\right\} = 0. \tag{1}$$

In deriving this equation, we assume that small-signal quantities vary as $\exp[j(\omega t-kz-\ell\theta)]$. Primes denote differentiation with respect respect to r, $\omega_c \equiv qB_0/m$, and $\omega_d \equiv \omega - kv_{0z} - \ell\Omega$, a complex function of r. To test the stability of this system, we assume real values of k and ℓ and try to find complex values of ω for which eigenfunctions, ϕ, exist that satisfy the boundary conditions.

In general, this analysis must be performed numerically. This numerical work can be aided considerably, or even avoided, if we perform some preliminary mathematical analysis in an attempt to answer two questions.

1. Are there certain values or functions that the equilibrium quantities can assume which are sufficient to ensure stability?
2. If the system is potentially unstable, can we limit the possible values of ω to some finite region of the complex ω-plane?

We shall employ various techniques used in the study of fluid hydrodynamics[4, 5] in this attempt. The basic method is to obtain quadratic forms that can be used to bound complex ω.

In Eq. 1, let

$$\phi(r) = [\omega_d(r)]^{1-n}\,\psi(r).$$

To place the resulting equation in self-adjoint form, multiply by ψ^* and integrate from $r = 0$ to $r = b$. The result is

$$\int_0^b r\omega_d^{2(1-n)}\,|\psi'|^2\,dr + \int_0^b |\psi|^2\,dr\left\{r(1-n)(kv''_{0z}+\ell\Omega'')\,\omega_d^{1-2n} + rn(1-n)(kv'_{0z}+\ell\Omega')^2\,\omega_d^{-2n} + (1-n)(kv'_{0z}+\ell\Omega')\,\omega_d^{1-2n} + r\omega_d^{2-2n}\left(\frac{\ell^2}{r^2}+k^2\right) - rk^2\omega_p^2\omega_d^{-2n}\left[1-\frac{\ell v'_{0z}}{kr\omega_c}\right] + \frac{\ell\left(\omega_p^2\right)'}{\omega_c}\,\omega_d^{1-2n}\right\} = 0. \tag{2}$$

This transformation requires that the velocity be defined in the space between the beam edge and the wall. We define this as the velocity that an electron would have if it were located in this region.

We now choose particular values of n to enable us to cast the imaginary part of Eq. 2 in various useful forms.

$\underline{n = \frac{1}{2}}$

If $n = \frac{1}{2}$ and $\omega_i \neq 0$, the imaginary part of Eq. 2 is

$$\int_0^b |\psi|^2 \left\{ \frac{\frac{1}{4}(kv'_{0z}+\ell\Omega')^2 - k^2\omega_p^2\left(1 - \frac{v'_{0z}}{kr\omega_c}\right)}{|\omega_d|^2} \right\} r\,dr = \int_0^b r\,dr \left\{ |\psi'|^2 + \left(\frac{\ell^2}{r^2} + k^2\right)|\psi|^2 \right\}. \tag{3}$$

But, if we use the calculus of variations, we can show that for any ψ which is zero at $r = b$, is finite otherwise, and for which $r\psi' = 0$ at $r = 0$,

$$\left[k^2 + (j_{|\ell|}/b)^2\right] \int_0^b |\psi|^2\, r\,dr \leqslant \int_0^b r\,dr \left[|\psi'|^2 + \left(\frac{\ell^2}{r^2} + k^2\right)|\psi|^2\right]. \tag{4}$$

In this formula, $j_{|\ell|}$ is the first zero of the Bessel function $J_{|\ell|}(r)$. By using this inequality, it follows that somewhere in the region $0 \leqslant r \leqslant b$

$$\omega_c^2 \leqslant |\omega_d|^2 \leqslant \frac{\frac{1}{4}(kv'_{0z}+\ell\Omega')^2 - k^2\omega_p^2\left(1 - \frac{\ell v'_{0z}}{kr\omega_c}\right)}{k^2 + (j_{|\ell|}/b)^2}, \tag{5}$$

and hence

$$\omega_i^2 \leqslant |\omega_d|^2 \leqslant \frac{\max\left\{\frac{1}{4}(kv'_{0z}+\ell\Omega')^2 - k^2\omega_p^2\left(1 - \frac{\ell v'_{0z}}{kr\omega_c}\right)\right\}}{k^2 + (j_{|\ell|}/b)^2}. \tag{6}$$

Equation 6 implies that a sufficient condition for stability is that everywhere

$$\frac{1}{4}(kv'_{0z}+\ell\Omega')^2 \leqslant k^2\omega_p^2\left(1 - \frac{\ell v'_{0z}}{kr\omega_c}\right). \tag{7}$$

If the system is unstable, then the eigenfrequencies must be confined to the region shown in Fig. VIII-17.

In particular, in Eq. 7 we can let $\ell = 0$ (or equivalently $|\omega_c| \to \infty$) and obtain our previous result[1] that a sufficient condition for stability is that everywhere

$$v'_{0z} \leqslant 2\omega_p.$$

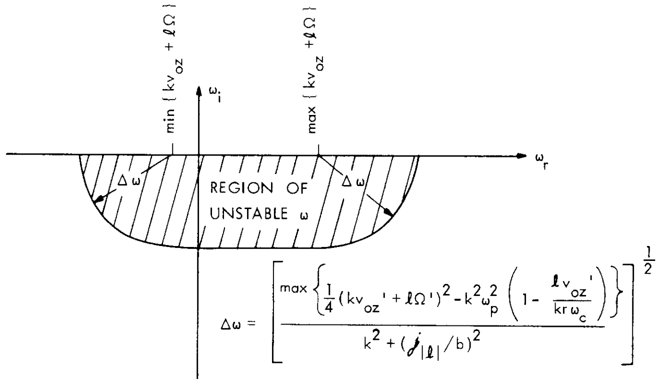

Fig. VIII-17. Locus of unstable ω.

Furthermore, if $v_{0z} \equiv 0$, we obtain the result that the beam is stable if everywhere

$$\frac{k}{\ell} \geqslant \frac{\Omega'}{2\omega_p}.$$

This equation is equivalent to one derived by Linson[6] for the case of a slab beam with constant density.

n = 0

If we set n = 0 in Eq. 2 and take the imaginary part, we can solve for ω_r:

$$\omega_r = \frac{\int_0^b 2r(kv_{0z}+\ell\Omega)\left[|\psi'|^2+\left(\frac{\ell^2}{r^2}+k^2\right)|\psi|^2\right]dr}{\int_0^b 2r\left[|\psi'|^2+\left(\frac{\ell^2}{r^2}+k^2\right)|\psi|^2\right]dr}$$

$$-\frac{\int_0^b |\psi|^2\frac{d}{dr}\left[r(kv_{0z}'+\ell\Omega')+\frac{\ell\omega_p^2}{\omega_c}\right]dr}{\int_0^b 2r\left[|\psi'|^2+\left(\frac{\ell^2}{r^2}+k^2\right)|\psi|^2\right]dr}. \tag{8}$$

By using Eq. 4, we can bound ω_r so that it lies in the range

$$\min\left\{kv_{0z}+\ell\Omega\right\} - \mathrm{mpv}\left\{\frac{1}{r}\frac{d}{dr}\left[r(kv'_{0z}+\ell\Omega') + \frac{\ell\omega_p^2}{\omega_c}\right]\right\}\left[\frac{\frac{1}{2}b^2}{k^2b^2+(j_{|\ell|})^2}\right] \leqslant \omega_r$$

$$\leqslant \max\left\{kv_{0z}+\ell\Omega\right\} - \mathrm{mnv}\left\{\frac{1}{r}\frac{d}{dr}\left[r(kv'_{0z}+\ell\Omega') + \frac{\ell\omega_p^2}{\omega C}\right]\right\}\left[\frac{\frac{1}{2}b^2}{k^2b^2+(j_{|\ell|})^2}\right]. \tag{9}$$

In this equation we have defined

mnv = min {minimum negative value, 0}

mpv = max {maximum positive value, 0}.

n = 1

Finally, let n = 1 and take the imaginary part of Eq. 2:

$$\omega_i\int_0^b |\psi|^2\,dr\left\{\frac{-2r\omega_p^2(\omega_r-kv_{0z}-\ell\Omega)\left(1-\dfrac{\ell v'_{0z}}{kr\omega_c}\right)k^2+|\omega_d|^2\dfrac{\ell\left(\omega_p^2\right)'}{\omega_c}}{|\omega_d|^4}\right\}=0. \tag{10}$$

If $\omega_i \neq 0$, a necessary condition for instability is that somewhere in $0 \leqslant r \leqslant b$

$$2k^2\omega_p^2(\omega_r-kv_{0z}-\ell\Omega)\left(1-\frac{\ell v'_{0z}}{kr\omega_c}\right)+|\omega_d|^2\frac{\ell\left(\omega_p^2\right)'}{r\omega_c}=0. \tag{11}$$

We can solve this for $\omega_r - kv_{0z} - \ell\Omega$:

$$\omega_r - kv_{0z} - \ell\Omega = -\frac{k\omega_p^2(kr\omega_c-\ell v'_{0z})}{\ell\left(\omega_p^2\right)'} \pm \sqrt{\left[\frac{k\omega_p^2(kr\omega_c-\ell v'_{0z})}{\ell\left(\omega_p^2\right)'}\right]^2-\omega_c^2}. \tag{12}$$

Since $\omega_r - kv_{0z} - \ell\Omega$ must be real, we obtain the bound

$$\omega_i \leqslant \max\left|\frac{k\omega_p^2(kr\omega_c-\ell v'_{0z})}{\ell\left(\omega_p^2\right)'}\right|. \tag{13}$$

Similarly, by solving for ω_i, it must follow that

$$\min\left\{kv_{0z}+\ell\Omega\right\} - \text{mpv}\left\{\frac{2k\omega_p^2(kr\omega_c-\ell v_{0z}')}{\ell(\omega_p^2)'}\right\} \leqslant \omega_r$$

$$\leqslant \max\left\{kv_{0z}+\ell\Omega\right\} - \text{mnv}\left\{\frac{2k\omega_p^2(kr\omega_c-\ell v_{0z}')}{\ell(\omega_p^2)'}\right\}.$$

Again, some previously known theorems are included here. In Eq. 11, let $k = 0$. Then the Rayleigh inflection point theorem will result. It states that a necessary condition for instability is that somewhere in the beam

$$\frac{\ell\left(\omega_p^2\right)'}{r} = 0.$$

Also, if we let $\ell = 0$, we obtain our previously proved theorem[1] that a necessary condition for instability is that somewhere in the beam

$$\omega_r - kv_{0z} = 0.$$

For practical use in the general case, Eq. 6 yields the most easily obtained and tightest bounds for use in numerical work. The other theorems, while of interest, are presented here primarily to illustrate the techniques used so that they may be applied to other problems.

J. A. Rome

References

1. R. J. Briggs and J. A. Rome, "Stability of Electron Beams with Velocity Shear," Quarterly Progress Report No. 90, Research Laboratory of Electronics, M. I. T., July 15, 1968, pp. 106-107.
2. J. A. Rome and R. J. Briggs, "Stability of Electron Beams with Velocity Shear," Quarterly Progress Report No. 97, Research Laboratory of Electronics, M. I. T., April 15, 1970, pp. 69-76.
3. I. I. Zhelyazkov and A. A. Rukhadze, "Instability of an Electron Beam with a Velocity Gradient," Soviet Phys. – Tech. Phys. 15, 188 (August 1970).
4. P. G. Drazin and L. N. Howard, "Hydrodynamic Stability of Parallel Flow of Inviscid Fluid," *Advances in Applied Mechanics* Vol. 9, p. 62, 1966.
5. D. D. Joseph, "Eigenvalue Bounds for the Orr-Sommerfeld Equation," J. Fluid Mech. 33, Part 3, 617-621 (1968).
6. L. M. Linson, "Space Charge Waves in Non-neutral Bound Plasmas," Bull. Am. Phys. Soc. 13, 1497 (1968).

4. DIRECT CONVERSION OF CHARGED-PARTICLE ENERGY FROM ENERGETIC PLASMAS

Introduction

The development of efficient methods for the conversion of charged-particle energy to electrical energy would have important consequences in the controlled-fusion program.[1,2] A basic difficulty in direct conversion from fusion plasmas is the broad range of energies present in the escaping plasma particles; a system must be devised that will remove a substantial fraction of the particle's kinetic energy, even though the initial energy of individual particles varies considerably.

In this report we consider a scheme based on the interaction of a tenuous plasma stream with a traveling wave set up by a lumped-element transmission line.[3] Primarily, we have in mind the plasma regimes of current interest for mirror machines,[1,2] namely plasma densities just beyond the mirror throat of the order of 10^8 cm^{-3}, average ion energies (T_i) of several hundred kilovolts, and electron temperatures $T_e \sim 0.1\ T_i$. (The basic ideas, of course, could be applicable to a variety of configurations and plasma regimes.) In this low-density, high-temperature regime, a quasi-electrostatic wave with a phase velocity much less than the electron thermal speed can penetrate a significant distance into the plasma (of the order of 0.5 m or so). The plasma escaping from the mirror ($B \sim 100$ kG) is adiabatically brought out into a weaker field region ($B \sim 1$-10 kG); and the perpendicular ion energy is thereby converted almost entirely into parallel energy. The plasma flow is now located inside a decelerating traveling potential well set up by the transmission line; the initial phase speed of the wave is synchronous with the fastest ions in the distribution. As we progress down the system, the wave speed slows down while the amplitude of the potential well builds up; the decelerating well therefore "sweeps down" the ion velocity distribution, trapping the ions and slowing them down to a much lower velocity. The electrons are never synchronous with the wave; however, their average energy is much less than the ions and need not be recovered, since in equilibrium the flow must have $\langle v_e \rangle = \langle v_i \rangle$ and equal densities.

This scheme does require plasma densities that are low enough to allow electrostatic fields to penetrate the plasma. In a higher density regime, we might consider using a traveling "magnetic well" with the equivalent potential $= -\mu B$ (μ = magnetic moment).

This intuitive picture of energy recovery by a decelerating wave is verified by the following analysis, and criteria for the necessary tapering of the potential amplitude and phase velocity of the wave are derived.

Deceleration of Particles by a Traveling Potential Well

A nonrelativistic particle of mass m and charge q is confined to motion in only one dimension, z, by a large magnetic field. The magnitude of the traveling electric field, $E_m(z)$, and its phase velocity, v(z), have adiabatic spatial variation properties. The equation of motion is

$$\ddot{z}(t) = \frac{q}{m} E_m(z) \sin \phi, \tag{1}$$

where

$$\phi = \int_{z_0}^{z} \frac{\omega\, dz'}{v(z')} - \omega t + \phi_o, \tag{2}$$

and the initial conditions are $z(o) = z_o$, $\dot{z}(o) = v_{po}$, and $\phi(o) = \phi_o$, the initial phase relative to the wave. We define normalized variables

$$\underline{t} = \omega t, \qquad \underline{z} = \frac{\omega z}{v(o)}, \qquad \underline{v}(z) = \frac{v(z)}{v(o)}, \qquad \gamma(z) = \frac{qE_m(z)}{m\omega v(z)}.$$

In terms of these variables, Eq. 1 can be written in the form

$$\frac{d^2\phi}{d\underline{t}^2} + \frac{d\underline{v}}{d\underline{z}} \left[1 + \frac{d\phi}{d\underline{t}}\right]^2 - \gamma(\underline{z}) \sin \phi = 0. \tag{3}$$

$$\frac{d\underline{z}}{d\underline{t}} = \underline{v} \left[1 + \frac{d\phi}{d\underline{t}}\right]. \tag{4}$$

If we multiply Eq. 3 by $d\phi/d\underline{t}$, we can derive an "energylike" expression in the form

$$\frac{d}{d\underline{t}} (T+V) = P, \tag{5}$$

where

$$T = \frac{1}{2} \left(\frac{d\phi}{d\underline{t}}\right)^2$$

$$V = \gamma(\underline{z}) \cos \phi + \phi \frac{d\underline{v}}{d\underline{z}}$$

$$P = \underline{v}\left(1+\frac{d\phi}{d\underline{t}}\right)\left(\phi\frac{d^2\underline{v}}{d\underline{z}^2}+\cos\phi\frac{d\gamma}{d\underline{z}}\right)-\frac{d\underline{v}}{d\underline{z}}\left(\frac{d\phi}{d\underline{t}}\right)^2\left(2+\frac{d\phi}{d\underline{t}}\right).$$

Note that if the velocity and field amplitude were constant in z, then P is zero, and we have the usual picture of a particle moving in a potential well (V) with kinetic (T) plus potential energies (in the wave frame) equal to a constant. For very slow variation in $\underline{v}(z)$ and $\gamma(z)$, we can picture the motion, according to (5), as a particle moving in a slowly varying well with a "dissipation" P(t) slowly changing the total energy.

For slowly varying $\underline{v}$ and γ, we can make a linear approximation around $\underline{z} \approx \underline{z}_o$ as

$$\underline{v}(z) = \underline{v}(\underline{z}_o) - \alpha(\underline{z}-\underline{z}_o)$$

$$\gamma(\underline{z}) = \beta[1+C(\underline{z}-\underline{z}_o)], \tag{6}$$

where

$$\alpha = -\left.\frac{d\underline{v}}{d\underline{z}}\right|_{z=z_o}, \quad \beta = \gamma(z_o), \quad C = \frac{1}{\beta}\left.\frac{d\gamma}{d\underline{z}}\right|_{z=z_o}.$$

If we now put the first-order term in γ on the right-hand side of Eq. 5, then the potential is

$$V(\phi) = \beta\cos\phi - \alpha\phi \tag{7}$$

and the new "dissipation function" (P) vanishes when the "velocity" ($d\phi/d\underline{t}$) vanishes. This implies that the ϕ coordinates of the minima (or maxima) of $V(\phi)$ are true stable (or unstable) "equilibrium points" throughout the domain where the linear approximation, Eq. 6, is applicable.

For particles with very small $\dot{\phi}$, and ϕ located near the minima of V, we could expand sin ϕ about that equilibrium point and proceed with a small-amplitude oscillation theory.[4] Using the adiabatic invariant of this simplified equation of motion, we find that in order for the amplitude of the phase oscillations about the equilibrium value to remain fixed we must have γ increasing according to the law

$$\gamma(z) = \text{const.}\ [v(z)]^{-4}. \tag{8}$$

This gives some idea of the relation between $E_m(z)$ and $v(z)$ required to keep particles with small oscillations trapped. But how particles become trapped is not predicted by the analysis.

An approximate analytical model for analyzing the transition from trapped to untrapped particle orbits was developed with the following physical reasoning. A particle with a velocity less than the local phase speed of the wave has $\dot{\phi} < 0$; this particle travels in the negative ϕ direction in the potential well $V(\phi)$ with an equivalent "dissipation" P (which can be negative) slowly changing its total energy (see Fig. VIII-18. To become trapped, a particle with $\dot{\phi} < 0$ must pass over the potential hump at $\phi = \phi_2 = 2\pi - \frac{a}{\beta}$, say, and not be able to clear the potential hill at $\phi = -\frac{a}{\beta}$. The particle will then be reflected, and travel back toward $\phi = \phi_2$; it will become trapped only if the net dissipation ($\oint$ P dt) is sufficient to put it below the potential hill at $\phi = \phi_2$. Our basic approximation is to use the zero-order particle orbit (valid in the limit of constant v and γ),

$$\frac{1}{2}\left(\frac{d\phi}{dt}\right)^2 + \beta \cos \phi = \text{const.}, \tag{9}$$

in calculating $\oint$ P dt.

Performing these calculations, we find that the condition for a particle that just clears the hill at ϕ_2 (that is, with $d\phi/dt \simeq 0$ at $\phi = \phi_2$) to just become trapped when it gets back to the peak of the hill (at $\phi = \phi_2$) is $\lambda = 4$, where

$$\lambda \equiv \left[\frac{\gamma'/\gamma}{-v'/v}\right]_{z=z_0} \tag{10}$$

With $\lambda > 4$, some of the particles will be trapped. With

$$\lambda \geqslant \lambda_{\max} = \frac{2\pi + 16\sqrt{\beta} + 4\pi\beta}{4\sqrt{\beta} + 2\pi\beta} \tag{11}$$

(and $\beta \lesssim 0.5$) essentially all of the particles will be trapped. This condition ($\lambda = \lambda_{\max}$) is the condition for a particle that is reflected at the peak of the hill at $\phi \approx 0$ to "lose enough energy" in one transit from 0 to 2π to become trapped. We are, at present, determining the percentage trapping for λ in the range between 4 and $\lambda_{\max}$; it appears that a rather substantial number (> 50%) are trapped for λ not very much larger than 4, as long as the velocity gradient is smooth enough ($a \sim 10^{-2}$ to 10^{-3}). It is also interesting to note that the $\lambda > 4$ condition is identical to the condition for damping of the small-amplitude oscillation (Eq. 8).

The preceding analysis was accomplished by assuming adiabatic variation of the field during one oscillation of a trapped particle. This method is approximate and valid for only a small region of parameter space. In order to verify the theory in this region and to investigate nonadiabatic effects, we have performed numerical integrations of the basic equation of motion for a variety of parameters. Some representative numerical

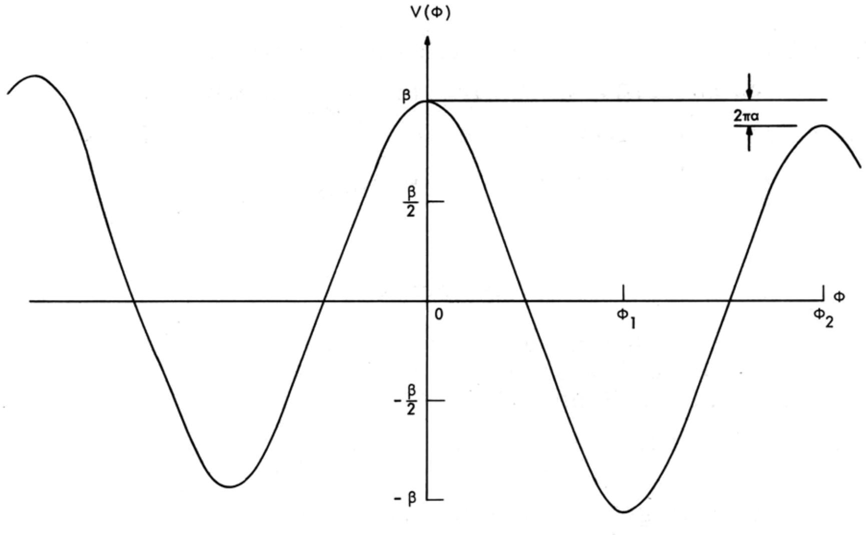

Fig. VIII-18. Potential function, $V(\phi) = \beta \cos \phi - \alpha\phi$. $\left(\phi_1 = \pi + \frac{\alpha}{\beta},\ \phi_2 = 2\pi - \frac{\alpha}{\beta}\right)$.

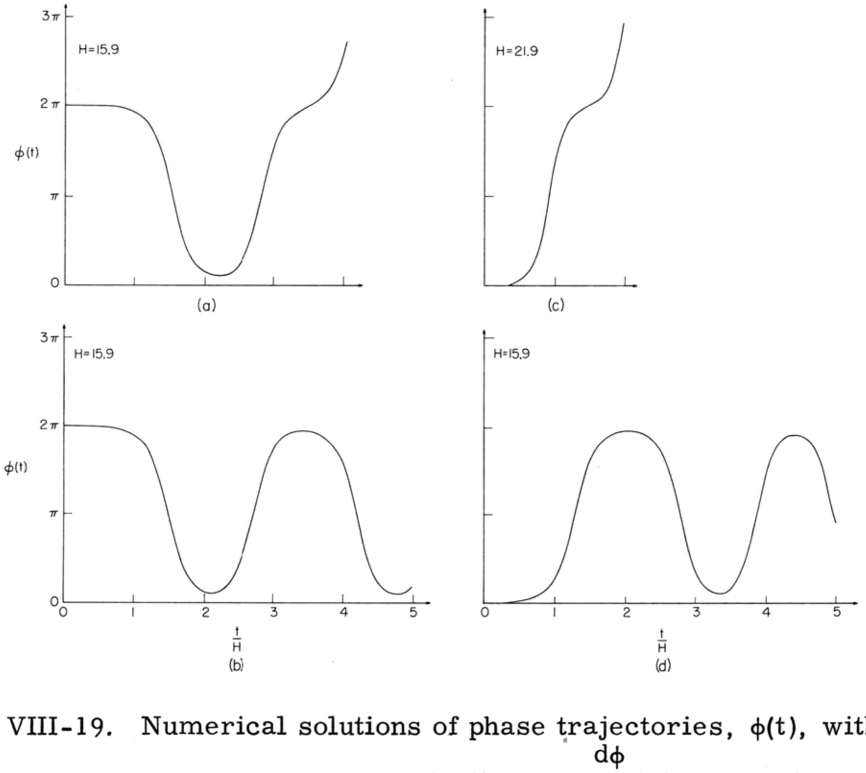

Fig. VIII-19. Numerical solutions of phase trajectories, $\phi(t)$, with the parameters $\alpha = 0.001$, $\beta = 0.1$, $\frac{d\phi}{d\underline{t}}(o) = 0$, $\underline{z}(o) = 0$.

(a) $\phi(o) = 6.27$, $\lambda = 3.0$
(b) $\phi(o) = 6.27$, $\lambda = 5.0$
(c) $\phi(o) = 0.0$, $\lambda = 7.0$
(d) $\phi(o) = 0.0$, $\lambda = 8.0$.

solutions of the phase trajectories of particles are shown in Fig. VIII-19. The trajectories in Fig. VIII-19a and VIII-19b confirm that λ_{min} is within the range of 3.0 to 5.0 for the particular conditions given. From Fig. VIII-19c and VIII-19d, we see that λ_{max} is between 7.0 and 8.0, where Eq. 11 predicts $\lambda_{max} = 6.7$ for those conditions.

M. I. Mirkin, R. J. Briggs

References

1. R. F. Post, "Mirror Systems: Fuel Cycles, Loss Reduction, and Energy Recovery," Proc. International Conference on Nuclear Fusion Reactors, Culham Laboratory, Culham, England, September 1969.
2. "Preliminary Report of Direct Recovery Study," UCID-15650, Lawrence Radiation Laboratory, Livermore, California, May 15, 1970.
3. H. A. Haus, "Alternating-Current Generation with Moving Conducting Fluids," J. Appl. Phys. <u>33</u>, 2161-2172 (1962).
4. A. D. Vlasov, "Theory of Linear Accelerators" (translated from Russian by Z. Lerman) Program for Scientific Translations, Jerusalem, Israel, 1968.

VIII. APPLIED PLASMA RESEARCH[*]

B. Plasma Physics and Engineering

Academic and Research Staff

Prof. R. A. Blanken
Prof. T. H. Dupree
Prof. E. P. Gyftopoulos
Prof. L. M. Lidsky
Dr. E. Oktay

Graduate Students

G. W. Braun
D. L. Cook
J. C. Hsia
B. H. Hui
D. S. Komm
T. A. Moulia
A. Pant
C. A. Primmerman
J. E. Robinson

1. FEEDBACK EFFECTS ON A LARGE-AMPLITUDE INSTABILITY IN A RADIOFREQUENCY DISCHARGE

This report gives experimental results and techniques for feedback stabilization of a large-amplitude instability; in particular, the relation between wave amplitude and feedback-loop gain phasing is examined.

The main point of these experimental results will be to show that in the high-gain regime the instability locks in, at a region near zero phase, to the feedback signal for all applied feedback phase shifts.

Reports on feedback stabilization of small-amplitude, single-mode instabilities have been reported previously.[1,2] When many modes are present simultaneously, and are of large amplitude the problem becomes more complex.[3-5] In this case it is difficult to interpret results using a simple feedback loop consisting of a wideband amplifier and a delay line. For example, when applying negative feedback to the $m = 1$ mode we are concurrently applying positive feedback to the $m = 2$ mode, and these modes can couple in the plasma. This provides a difficult problem if the coupling mechanism is unknown.

The instability studied in this experiment occurs in a previously reported experiment.[6] The instability is observed at a magnetic field of 600 G. It is a large-amplitude ($\tilde{n}/n \sim 0.35$), "drag-type" instability[7-9] located 3-4 cm from the column axis (see also Sec. VIII-B.2). It occurs at low neutral pressures ($1-2\times10^{-5}$ Torr Argon) and for large electron temperatures in the central region of the column (5-10 eV). The wave is a single azimuthal perturbation that rotates in the electron diamagnetic direction with a phase velocity of 5.6×10^4 cm/s. The waveform is nonsinusoidal; the Fourier analysis is shown in Fig. VIII-20. While it is not a multimode instability, it has similar inherent problems with respect to feedback stabilization, as can be observed from the spectrum.

---

[*] This work is supported by the National Science Foundation (Grant GK-18185).

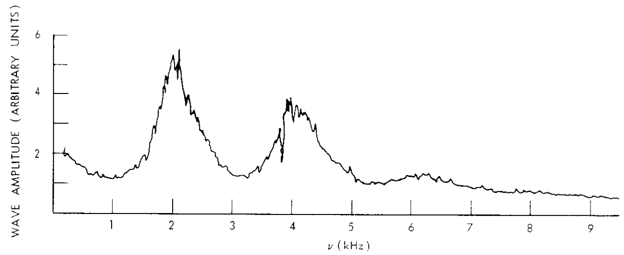

Fig. VIII-20. Frequency spectrum of ion saturation current fluctuations.

In this experiment we decided to use filters and to examine the effect of feedback of the first harmonic on the instability. This avoids the possibility of exciting other modes directly. Filters are used, however, at the expense of a greatly increased time delay through the feedback system. The instability, therefore, must have a correlation time greater than the time delay through the system if application of feedback is to have any effect.

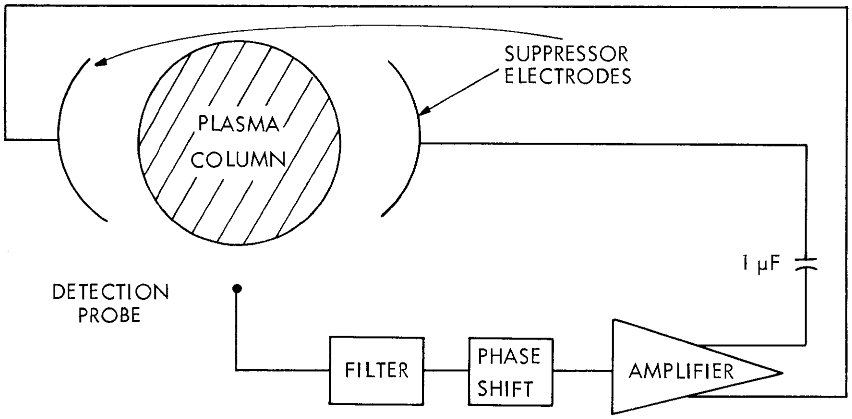

Fig. VIII-21. Feedback loop.

The feedback circuit is shown in Fig. VIII-21. The filters were calibrated and the damping adjusted so that the bandpass for the entire feedback circuit was centered at 2 kHz with a full width at half-maximum of 900 Hz. Measurements of the time response of the circuit, using a 2-kHz tone burst showed a 1-ms time delay for the signal to decay to half of its original amplitude. At instability frequency of 2 kHz this delay time amounts to 2 cycles. The correlation function for this instability was measured and found to have a decay time of more than 8 cycles. On this basis, the feedback is expected to retain meaningful phase information even if delayed 2 cycles.

The suppressor electrodes are rectangular plates (1×2 cm) radially positioned at the maximum wave amplitude and azimuthally separated by 180° (Fig. VIII-21).

The detection probe was located approximately 1 m axially from the electrodes and positioned radially near the maximum wave amplitude. Care was taken in locating this position so that no resistive pickup was obtained directly from the electrodes. This was accomplished by applying a noncoherent, large-amplitude, 9 kHz signal to the electrodes, and then positioning the detection probe so that it did not see this signal. The 9-kHz signal was far enough from the natural frequencies of the plasma that it did not elicit a wave type of response.

Data were taken for one electrode driven with reference to ground and for two electrodes driven out of phase. The latter will be presented in this work as both sets are qualitatively similar.

Figure VIII-22a shows the wave amplitude as a function of corrected phase with the gain of the feedback loop as a parameter. At low gains the amplitude dependence has a continuous sinusoidal character. The frequency shift at low gains exhibits the same

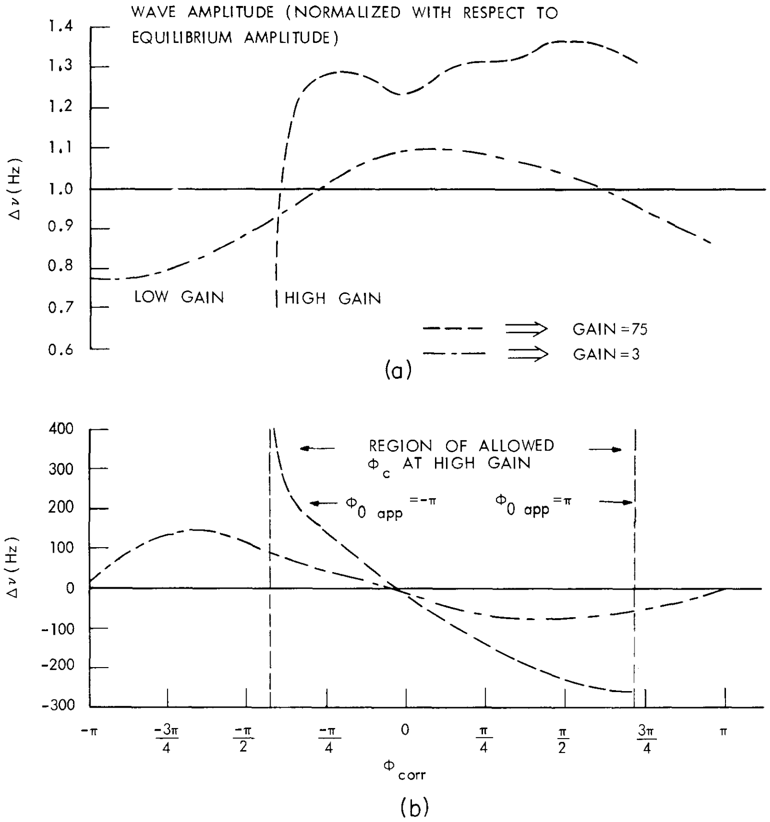

Fig. VIII-22. (a) Normalized wave amplitude for high and low gains as a function of ϕ_{corr}.

(b) Frequency shift $\Delta\nu$ for high and low gains as a function of ϕ_{corr}. Since the phase shift is a function of frequency, $\phi_{corr} = \phi_{app}(\nu_o+\Delta\nu)$; $\phi_{o\ app} = \phi_{app}(\nu_o)$.

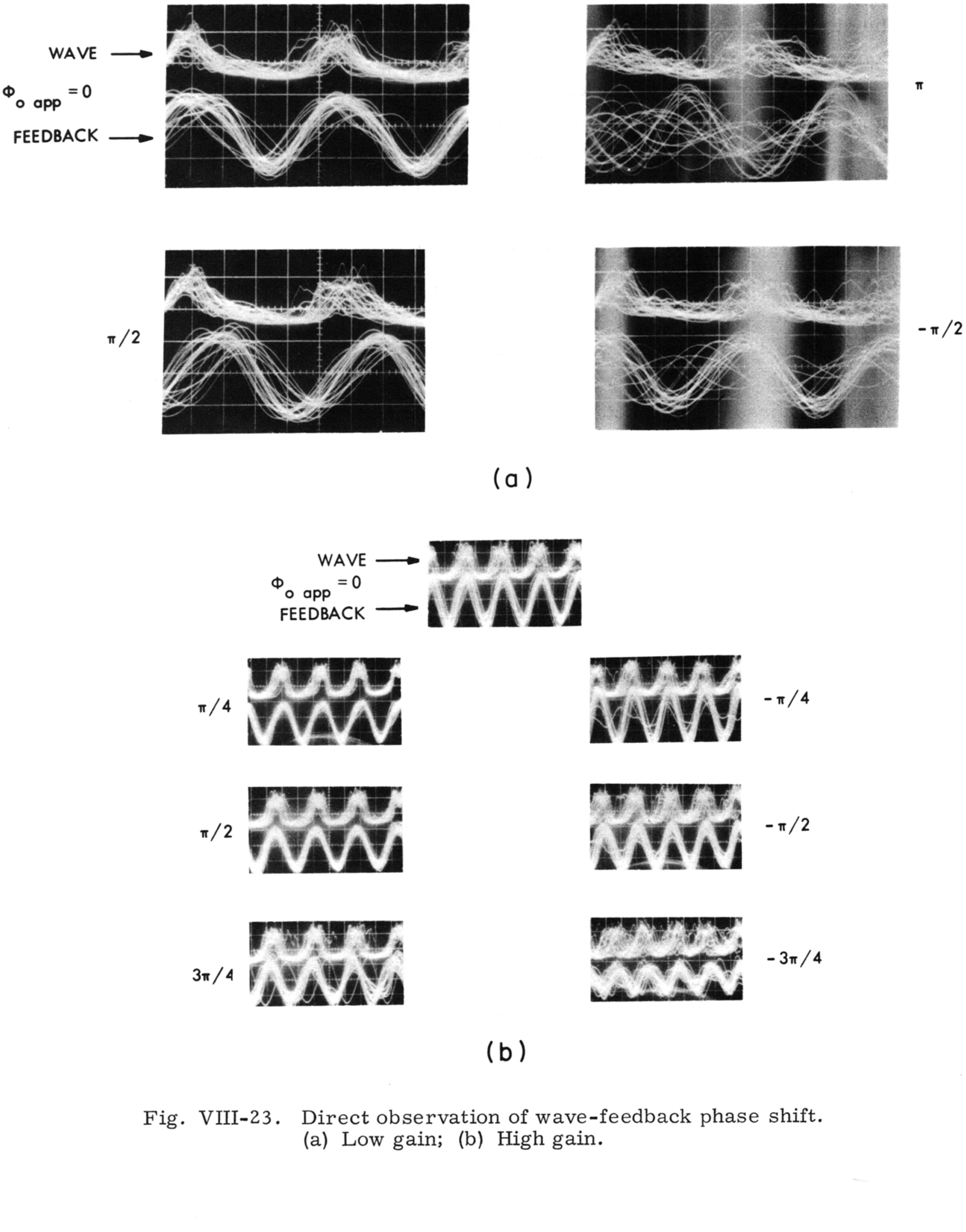

Fig. VIII-23. Direct observation of wave-feedback phase shift. (a) Low gain; (b) High gain.

properties (Fig. VIII-22b). Figure VIII-23a shows the actual phase shift between the wave and the applied feedback signal at low gains. It should be observed that the applied signal in this low-gain case shifts phase continuously, as $\phi_{\text{o app}}$ is varied, with respect to the wave.

In contrast, looking again at Fig. VIII-22, we can see that for the high-gain case the wave locks into the phase shift. This can be noted because, for the most part, change in the wave amplitude is relatively large and positive, indicative of the fact that the wave is maintaining a small phase shift with respect to the feedback signal. In Fig. VIII-22b the frequency shift can be seen as a continuously decreasing function of ϕ_{corr} until $\phi_{\text{o app}} = +\pi$ is reached, at which point $\Delta\nu$ makes a discontinuous jump back to its value at $\sim\phi_{\text{o app}} = -\pi$.

Looking at Fig. VIII-23b, we see that for all $\phi_{\text{o app}}$ such that $-\pi < \phi_{\text{o app}} < +\pi$ the actual phase shift between the wave and feedback signal is within $\pm\pi/2$.

The region about $\phi_{\text{o app}} = \pi$ is obviously unstable. This region, containing the discontinuous frequency shift can clearly be seen in Fig. VIII-24. The frequency shift is continuous for $-\pi < \phi_{\text{o app}} < +\pi$, but as $\phi_{\text{o app}}$ is varied across π there is a discontinuous jump from a frequency 300 Hz below to 400 Hz above ν_{o}.

In conclusion, a filtered feedback system has been used to study the effect of low-gain feedback stabilization and high-gain phase frequency entrainment. It has been

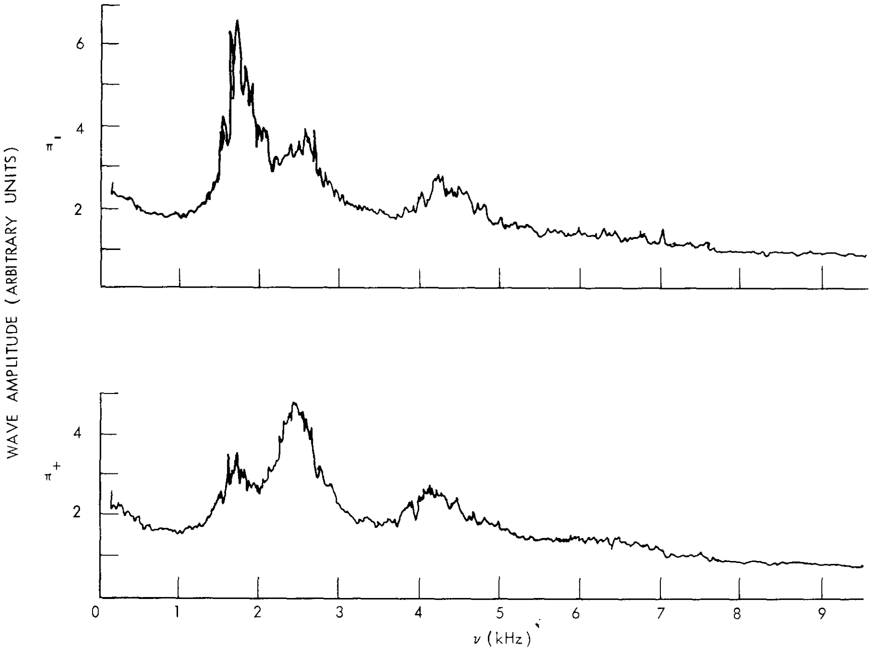

Fig. VIII-24. Frequency spectra showing discontinuous frequency transition at $\phi_{\text{o app}} = \pm\pi$.

observed that in the low-gain regime results are obtained which are qualitatively similar to those of Lindgren.[5] That suppression of only approximately 20% is achieved as indicative that this is an extremely large-amplitude wave. A similar problem was observed by Jassby.[3] It is worth noting that the low-gain results show a sinusoidal variation of amplitude with phase which is peaked at $\phi_{\text{corr}} = 0$. This is in contrast to reports by Muller[2] and Keen,[10] who noted an $(\text{amplitude})^2$ sinusoidal dependence, peaked at $\phi_{\text{corr}} = \pi/2$.

To explain this may require an exact knowledge of the wave feedback coupling mechanism. Physically, if we modified the energy content of the wave we should expect to see results such as those of Keen.[10] If, however, the symmetry is such that the wave is able to shift its azimuthal position with little or no loss in energy, then we might expect results such as those that we obtained at low gains.

When higher gains are applied in order to obtain better suppression, the wave merely frequency shifts $\Delta\nu$, so that at $\nu + \Delta\nu$ the actual phase shift seen by the wave $\phi_{\text{app}}(\nu+\Delta\nu) = \phi_{\text{corr}}$ is maintained near zero. This results in a generally enhanced amplitude at all phases, except near the unstable region $\phi_{\text{o app}} = \pm\pi$, and therefore suppression is unobtainable.

Further work will be done on the interpretation of these results.

T. A. Moulia

References

1. B. E. Keen and R. V. Aldridge, Phys. Rev. Letters 22, 1358 (1969).
2. G. L. Muller, J. C. Corbin, and R. S. Palmer, American Institute of Physics Conference Proceedings No. 1, Feedback and Dynamic Control of Plasmas, 1970.
3. D. L. Jassby, Ph.D. Thesis, Department of Astrophysical Sciences, Princeton University, 1970.
4. R. R. Parker and K. I. Thomassen, Phys. Rev. Letters 22, 1171 (1969).
5. N. E. Lindgren and C. K. Birdsall, American Institute of Physics Conference Proceedings No. 1, Feedback and Dynamic Control of Plasmas, 1970.
6. J. E. Robinson, E. Oktay, L. M. Lidsky, and R. A. Blanken, Quarterly Progress Report No. 97, Research Laboratory of Electronics, M.I.T., April 15, 1970, pp. 92-101.
7. A. Simon, Phys. Fluids 6, 382 (1962).
8. F. C. Hoh, Phys. Fluids 6, 1184 (1963).
9. D. L. Morse, Phys. Fluids 8, 1339 (1965).
10. B. E. Keen, Phys. Rev. Letters 24, 259 (1969).

2. TRANSVERSE KELVIN-HELMHOLTZ TURBULENCE IN A RADIOFREQUENCY DISCHARGE

Low-frequency transverse Kelvin-Helmholtz turbulence has been tentatively identified in a radiofrequency discharge.[1] In this report, additional experimental data are presented and compared with Kelvin-Helmholtz theory. Both hydrodynamic turbulence and a single coherent $m = 3$ mode have been observed in an azimuthally sheared region of the column. The hydrodynamic turbulence consists of small-scale sized clumps of plasma similar to eddies found in fluid turbulence. The coherent mode is similar to observations made in other experiments[2-4] and it can be compared with the theoretical models of Rosenbluth and Simon[5] and of Stringer and Schmidt.[6] Nonlinear effects are briefly discussed with reference to the hydrodynamic turbulence, the observation of a single coherent mode, and the general validity of the linear theory.[7,8]

Experimental System

The basic experimental system shown in Fig. VIII-25 was described in a previous report.[1] The Lisitano structure has been enlarged to an inner radius of 1.9 cm with 12 connected slots. It is fed with 25 W of 2800 MHz radiofrequency power in a magnetic field tuned for electron-cyclotron resonance heating. Less than 0.1 V/cm of radiofrequency field was measured in the experimental region when the discharge was operating. The neutral pressure was approximately $3\text{-}6 \times 10^{-4}$ Torr Argon in the source region and 5×10^{-5} Torr in the experimental region. At this frequency and pressure, the source

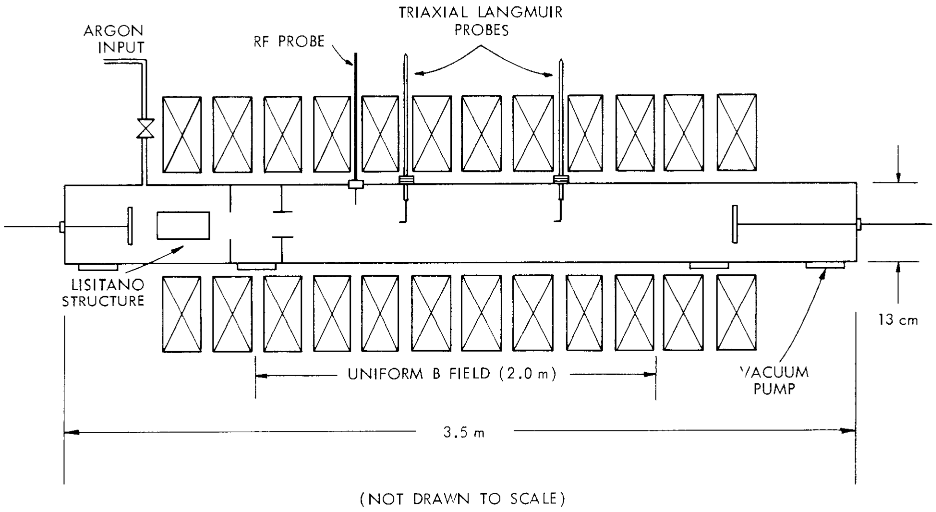

Fig. VIII-25. Experimental system.

magnetic field can be tuned to form a relatively uniform and azimuthally symmetric plasma column. The plasma parameters are the following: ion density, $1\text{-}2 \times 10^{10}$ cm^{-3}; electron temperature, 1-7 eV; and ion temperature, 0.2-0.3 eV (see Sec. VIII-B.3).

Cylindrical orbital-motion-limited Langmuir probes were used to measure plasma potential fluctuations, since they are less sensitive to electron temperature; that is, the correction factor between floating and plasma potential is approximately 2.8 T_e.[9, 10] They are triaxial and capacitance-neutralized with an input impedance of 10^7 Ω at 50 kHz.

Plasma Rotation and Shear

The dominant feature of the plasma column is an annular layer of warm electrons caused by the heating pattern of the Lisitano structure. By equating ion and electron end losses, we would expect that plasma potential would be peaked in this layer of maximum electron temperature. This was verified by plasma potential measurements as shown in Fig. VIII-26. The dashed line indicates the region in which the electron distribution is non-Maxwellian and the potential cannot be accurately measured. The potential is characterized by an inward-pointing electric field at small radii and a reversing field at larger radii. This results in a nonuniform $\underline{E} \times \underline{B}/B^2$ rotation of the

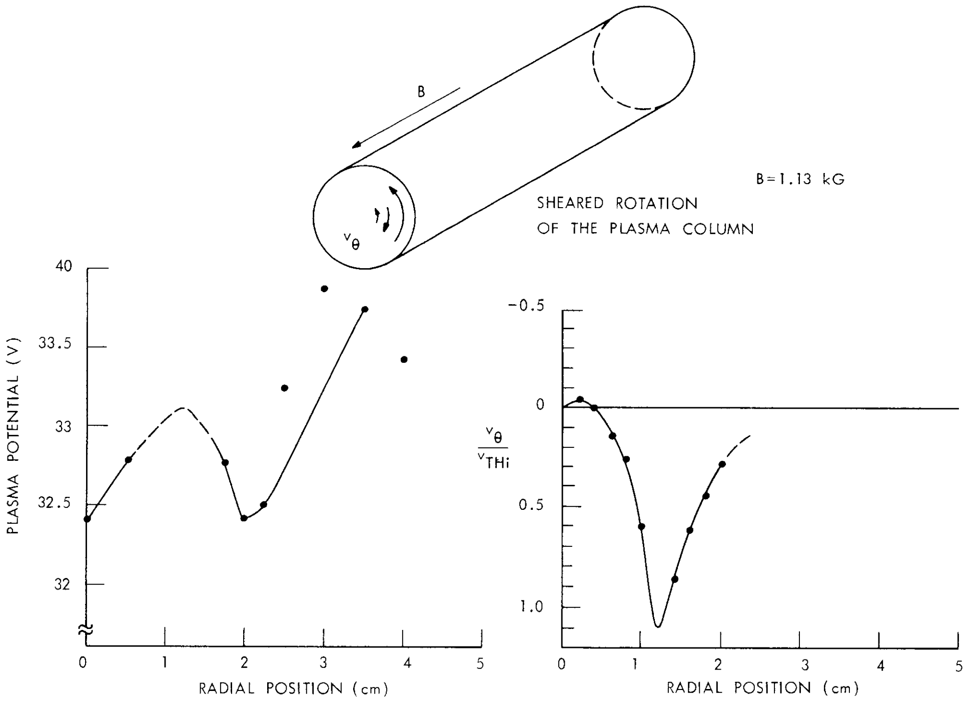

Fig. VIII-26. Plasma potential and direct rotation measurements.

plasma column and Kelvin-Helmholtz turbulence.

To verify the potential distribution, the rotation has been measured directly using a double-plane probe technique.[11] The directed velocity modifies the sheath and the resulting ion saturation current so that it changes in proportion to the drifting component of the ion temperature. For $V_D < V_s$ (the ion acoustic speed) and $a_i > R_p > 30\lambda_D$, the drift can be expressed as

$$V_D \approx + \frac{1}{4} (T_e/T_i) (\Delta I/I) \cdot V_{THi} \tag{1}$$

where I is the ion saturation current collected by one plate, and ΔI is the difference between collecting plates. A typical rotation curve is shown in Fig. VIII-26. It shows the rotation reversal within the spatial resolution limits of a Larmor radius and it shows a region of large rotation. For $T_i = 0.25$ eV this corresponds to approximately 10^3 m/s for the rotation. This value is in agreement with the measured potential distribution when using the following expression for rotation:

$$\langle v_\theta \rangle = -\frac{\omega_{ci} r}{2} + \frac{\omega_{ci} r}{2} \left[1 - \frac{4}{\omega_{ci} r} \frac{\langle E \rangle}{B} \right]^{1/2}, \tag{2}$$

where the radial electric field is averaged over the ion orbits.

Hydrodynamic Turbulence

Hydrodynamic turbulence is observed at small rotation rates ($v_e/v_{THi} \lesssim 0.6$) in the sheared layer of the plasma column. This corresponds to low magnetic field values in the experimental region (600 G). The turbulence is characterized by clumps of plasma exhibiting an approximate 1/f spectrum peaked near or lower than the maximum rotation frequency. The clumps propagate with the average $\underline{E} \times \underline{B}/B^2$ speed of the plasma but with a scale size of only a Larmor diameter. Figure VIII-27 shows typical autocorrelation and crosscorrelation data for the clumps. Two ion-collecting Langmuir probes are azimuthally separated 0.75 cm at a radius of 2.0 cm. A time delay and amplitude attenuation can be seen from the correlations to indicate a 3×10^2 m/s phase velocity and a 100-μs clump lifetime. Jassby has also reported hydrodynamic turbulence at these rotation rates, but the turbulence retained the characteristics of a multiple-mode spectrum similar to linear Kelvin-Helmholtz theory.[4] The turbulence observed here has a continuous spectrum and the scale size is less than the corresponding wave numbers (m/r). The turbulence is in a fully developed nonlinear state and resembles eddies observed in fluid turbulence. This could be the plasma analog of eddy formation in fluids. That is, in the fully developed nonlinear state the plasma breaks up into clumps with a scale size of the Larmor radius where strong turbulent and viscous damping can

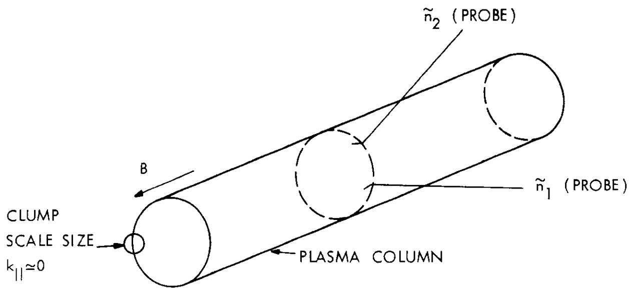

LANGMUIR PROBE ORIENTATION

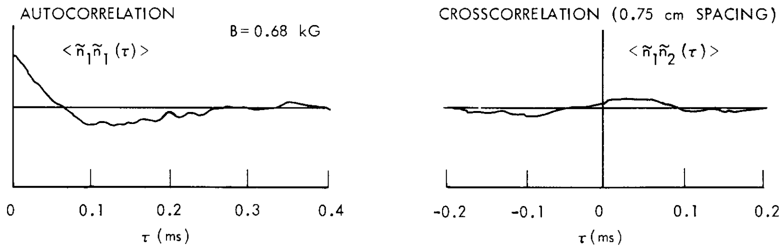

Fig. VIII-27. Hydrodynamic turbulence.

dissipate the clump energy ($K_\perp a_i \approx 1$).[7, 8] If the local potential fluctuations of a clump are sufficiently large, a local rotation reversal can occur and a vortex is formed. For this experiment the potential fluctuations are 0.5-1.0 V, sufficient to cause strong nonlinear dissipation and local vortex formation for some clumps.

The energy source for the hydrodynamic turbulence need not be the rotation, even though this would be a likely candidate because of the frequency spectrum, the localization of the turbulence, and the observation that $\tilde{\Phi}/T_e$ is greater than the normalized density fluctuations. Rather, the clumps could be the response of the plasma to another energy source.

Coherent Kelvin-Helmholtz Turbulence

Increasing the magnetic field from 600 G results in an increased rotation rate of the sheared layer with the simultaneous appearance of a coherent m = 3 mode as shown in Fig. VIII-28. The frequency, radial localization, phase velocity, and radial variation of potential fluctuation phase are in agreement with the theory for Kelvin-Helmholtz turbulence.

The radial wave equation has been derived from the Vlasov equation[5] and the fluid equations[6] to describe the guiding center motion of a particle in a sheared rotating plasma column in a magnetic field. The theory is valid for the following conditions:

$$\frac{a}{L} < 1, \qquad \frac{\omega_E}{m\omega_{ci}} \ll 1, \qquad \frac{\omega}{\omega_{ci}} \ll 1.$$

If this is satisfied, the radial wave equation has the following form without viscosity and finite $K_{\|}$:

$$\frac{d}{dr}\left\{nr^3(\omega-\omega_E)(\omega-\omega_E+\omega_{oi})\frac{d\psi}{dr}\right\} + \omega^2 r^2 \frac{dn}{dr}\psi$$
$$- \frac{m^2-1}{r^2}\, nr^3(\omega-\omega_E)(\omega-\omega_E+\omega_{oi})\,\psi = 0, \tag{3}$$

where ψ is the guiding center motion $\frac{m}{rB}\,\frac{\tilde{\Phi}}{\omega-\omega_E}$. It is assumed that $K_{\perp}a_i \ll 1$ and that finite Larmor radius effects come in as a damping term in the ion drift velocity.

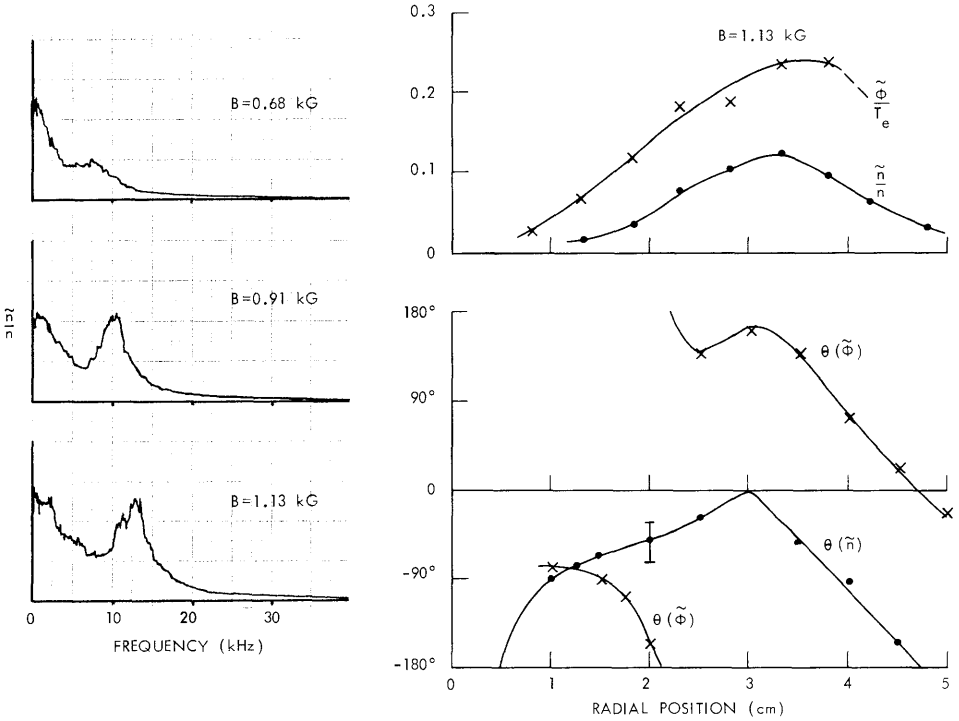

Fig. VIII-28. Coherent Mode.

The guiding center motion is related to the density and potential fluctuations by

$$\tilde{n}/n = -\frac{1}{n}\frac{dn}{dr}\psi \tag{4}$$

and

$$\tilde{\phi} = \frac{Br}{m}(\omega - m\omega_E)\psi. \tag{5}$$

It can be seen from these expressions that the potential fluctuations would be peaked at the maximum rotation in the shear layer and density fluctuations would be peaked at the maximum density gradient in the layer. Also, the potential fluctuations would exhibit a 180° phase shift in the shear layer.

Figure VIII-28 shows that $\tilde{\phi}$ is localized near the maximum rotation and that it undergoes a radial phase shift of approximately 180° in the shear layer. The phase velocity measurement shown in Fig. VIII-29 is in agreement with the linear theory. That is, the phase velocity is predicted by radially averaging the wave amplitude over the rotation of the column.[3, 4]

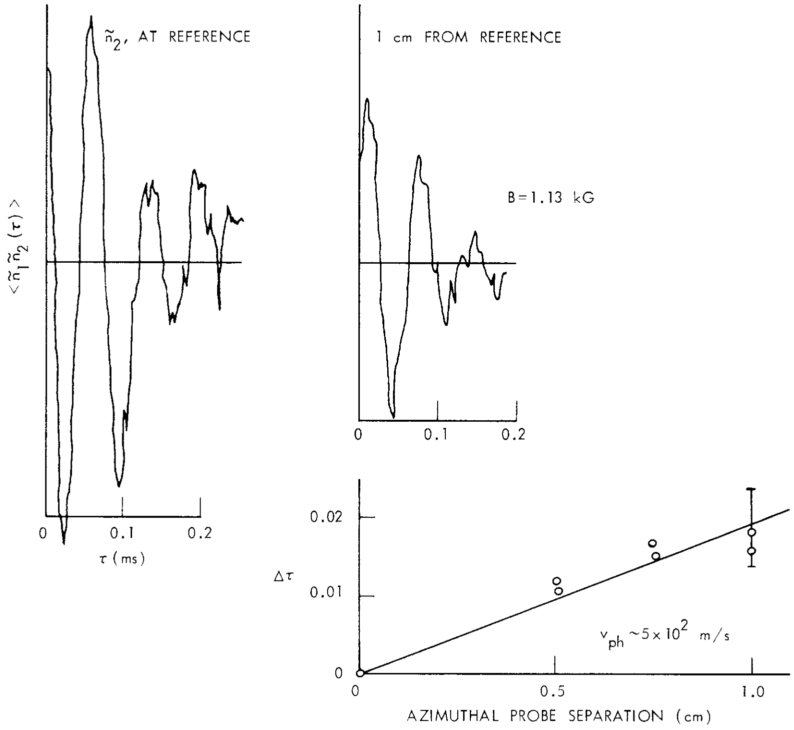

Fig. VIII-29. Phase velocity of the coherent mode.

The Richardson number indicting the effect of shear relative to rotation can be calculated for the m = 3 mode. That is,

$$T_c = \frac{1}{K_\perp^2 r}\,\frac{dn}{dr}\,\frac{1}{n}\,\frac{\bar{\omega}_E(\bar{\omega}_E - \bar{\omega}_{oi})}{(\delta\omega_E)^2} \approx -0.25. \tag{6}$$

Since $|T_c| < 1$, the growth rate is due mainly to the shear mechanism.[3, 4]

The observance of only a single mode can be explained with reference to the linear and nonlinear theory. Consider the solution to the radial wave equation. Solutions have been based on (a) a multiple layer model, and (b) radial integration of the equation to obtain a quadratic form in ω.[2-4] The second method is more accurate, but requires a knowledge of the radial distribution of the modes. In the first method an approximate mode solution is assumed which yields an approximate quadratic. By using three layers and assuming that $m \geqslant 2$, an approximate solution can be found based on the first method:

$$\omega_r \approx \frac{\delta(m^2-1)\,\alpha_2\omega_2}{1+\delta\alpha_2(m^2-1)/m} \tag{7}$$

and

$$\omega_i^2 \approx \frac{\delta(m^2-1)\,m\alpha_2\omega_i^2}{1+\delta\alpha_2(m^2-1)/m} - \omega_r^2, \tag{8}$$

where δ is the width of the shear layer normalized to the mean radius of the layer, α_2 is the density weighting factor for the shear layer, and ω_2 is the average frequency of the layer.

These expressions indicate a wide spectrum of unstable modes (10 modes). For $m = 3$, however, $K_\perp a_i$ is of order unity, and the linear theory approximation are not valid. It is not known whether the growth rate should increase for $K_\perp a_i \gg 1$, but these modes have not been observed experimentally. It might be expected that the growth rate would decrease or stay relatively constant with larger $K_\perp a_i$, because of finite Larmor radius effects. However, viscous damping increases with $(K_\perp a_i)^2$ and could damp the wave. The experiments of Kent[12] and those of Jassby,[13] when a_i is computed using the distorted radius that is due to the zero-order electric field, indicate that the spectrum has a maximum when $K_\perp a_i \approx 1$, or where a mode has the largest growth rate and has $K_\perp a_i \ll 1$. That is, for large radial electric fields the dominant mode has $K_\perp a_i$ of order unity. This can explain the observation of a single mode in this experiment, and mode switching and quenching in other experiments.

Non linear effects are thought to be important, since (i) the trapping condition is satisfied,

$$\frac{\phi K_r}{B} \gtrsim v_{pn}, \tag{9}$$

and (ii) turbulent scattering scales as $K_\perp^2 D_\perp$.[7, 8] This first condition is sufficient for trapping and scattering to dominate the particle perpendicular motion, while the second condition indicates that the high m number modes will be strongly damped similarly to viscous damping. That is, if the high m number modes are not suppressed by finite Larmor radius effects and viscous damping, the strong turbulence can account for their absence. The low m numbers (m=1,2) are thought to be attenuated by or masked by the hydrodynamic turbulence.

J. E. Robinson, L. M. Lidsky

References

1. J. E. Robinson, E. Oktay, L. M. Lidsky, and R. A. Blanken, Quarterly Progress Report No. 97, Research Laboratory of Electronics, M. I. T., April 15, 1970, pp. 92-101.
2. G. I. Kent, N. C. Jen, and F. F. Chen, Phys. Fluids 12, 2140 (1969).
3. D. L. Jassby and F. W. Perkins, Phys. Rev. Letters 24, 256 (1970); Phys. Fluids 14, 102 (1971).
4. D. L. Jassby, Ph. D. Thesis, Department of Astrophysical Sciences, Princeton University, 1970.
5. M. N. Rosenbluth and A. Simon, Phys. Fluids 8, 1300 (1965).
6. T. E. Stringer and G. Schmidt, Plasma Physics 9, 53 (1967).
7. T. H. Dupree, Phys. Fluids 10, 1049 (1967).
8. T. H. Dupree, Phys. Fluids 11, 2680 (1968).
9. J. G. Laframboise, Report 100, University of Toronto, Institute for Aerospace Studies, 1966.
10. F. F. Chen, C. Etievant, and D. Mosher, Phys. Fluids 11, 811 (1968).
11. M. Hudis and L. M. Lidsky, J. Appl. Phys. 41, 5011 (1970).
12. See ref. 2, Figure 10, on mode switching.
13. See ref. 4, Figures 32, 33, 34, on mode switching (a_i calculated including the applied radial electric field).

3. ION DOPPLER BROADENING MEASUREMENT IN A LOW-INTENSITY PLASMA

Introduction

A Fabry-Perot optical interferometer system has been assembled to measure ion temperature in the electron-cyclotron resonance (ECR) heated Argon plasma.[1] In this report, the over-all finesse of the optical system is discussed including the effect of aperture; and preliminary measurement of the broadening of A II 4610 Å line radiation emitted by the plasma is reported.

The intensity of optical radiation emitted by low-density ($N_e \approx 10^{10}-10^{11}$ cm^3) steady-state plasmas, for example, ECR heated plasmas, is very low. In optical studies of such plasmas it is necessary to use large aperture to obtain a workable level of signal output from the photomultiplier. The use of large aperture results, however, in significant system broadening of the observed line. Therefore the system broadening has to be determined and unfolded from the observed broadening to obtain the true broadening of the line emitted by the plasma.

Description of the Optical System

A schematic diagram of the optical system is shown in Fig. VIII-30. Radiation emitted by the plasma is collected by lens L_1 and focused on the aperture with diameter A. Lens L_2 collimates rays passing through A, and these nearly parallel rays are passed through the Fabry-Perot plates. An interference filter, with peak transmission

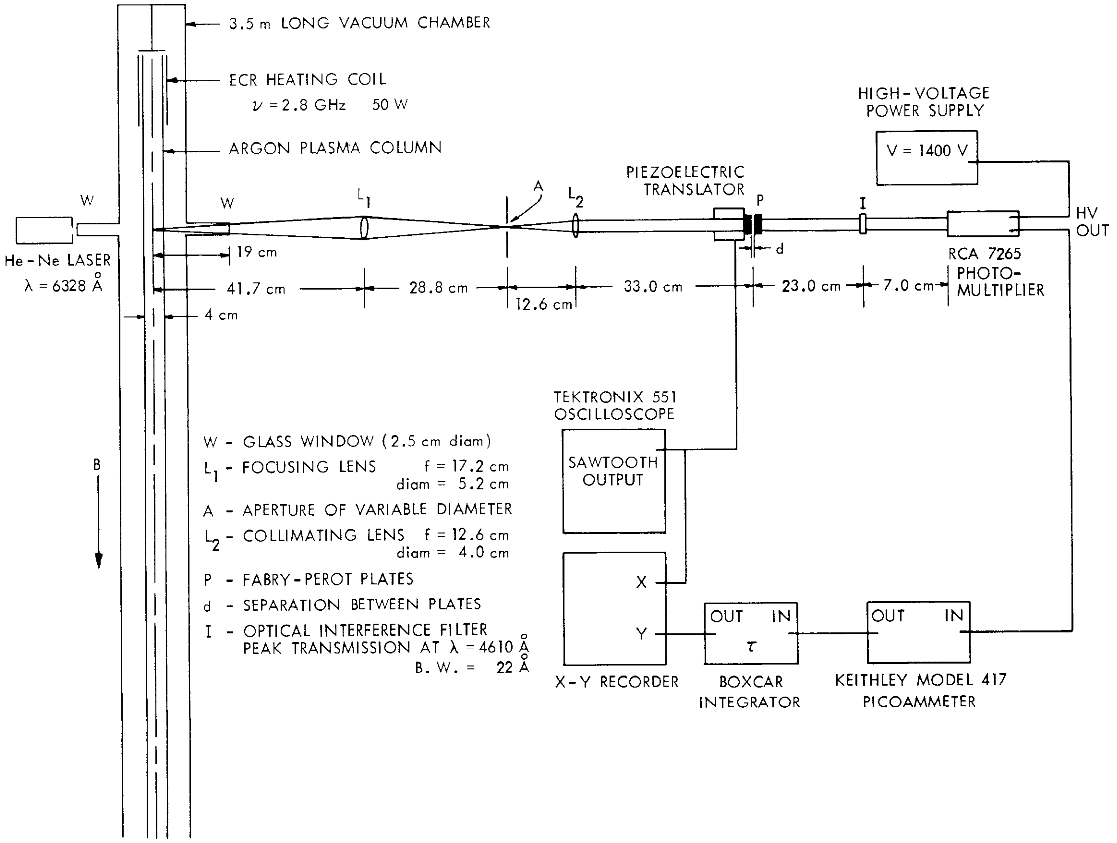

Fig. VIII-30. Optical system.

at λ = 4610 Å and a bandwidth of 22 Å is mounted ahead of the photomultiplier. The output of the photomultiplier is fed into a Keithley Model 417 picoammeter that has provision for suppressing the DC level. An integrator is used following the picoammeter to filter out noise attributable to the photomultiplier and the picoammeter. The output of the integrator is fed into the Y input of an X-Y recorder.

The interferometer is a Coherent Optics Model 360 interferometer that utilizes a piezoelectric translator to move one of the plates axially. The sawtooth output of a Tektronix 551 oscilloscope is used to drive this translator and also the X input of the X-Y recorder. The axial motion of one of the plates by λ/z produces a scan of one spectral range, $\Delta\lambda = \lambda^2/2d$, where d is the separation between the plates. The X-Y recording therefore represents a plot of wavelength against intensity of the transmitted radiation.

The Fabry-Perot plates, 1 in. in diameter, are 1/2 in. thick and their flatness figure is $\lambda/100$. They have broadband coatings with reflectivity, R, of approximately 0.97 to 0.985 for $\lambda = 4000$ to 6500 Å.

The He-Ne laser at the other side of the plasma is used to align the optical system and to measure the over-all system finesse.

Discussion of the "System" Finesse

There are three obstacles in measuring the broadening of the A II 4610 Å line emitted by the plasma.

1. ECR-heated plasma has low electron density ($N_e \approx 5 \times 10^{10}$ cm^{-3}). Therefore, the intensity of optical radiation emitted by the plasma is quite low; thus, the detection of the A II 4610 Å line is difficult.

2. As a consequence of low light intensity, there is a minimum value of A which can be used. The over-all system finesse is, however, inversely proportional to A^2. Therefore the aperture may contribute significantly to the observed broadening of the line.

3. The alignment of the optical system is very critical to the proper measurement of the line broadening. The aperture has to be exactly at the center of the collimating lens, L_2, and at its focal point. The Fabry-Perot plates have to be critically adjusted. In working with low-level light intensities, the alignment of the aperture, the collimating lens, and the Fabry-Perot plates by visual inspection[2,3] can be very misleading.

Finesse, F, is defined as the ratio of the free spectral range, $\Delta\lambda$, to the full width at half-intensity macimum (FWHM) of the line $\Delta\lambda_{1/2}$ (Fig. VIII-31). Three major factors contribute to F: (i) reflectivity of the plates, R; (ii) flatness of the plates, a; and (iii) aperture diameter, A. The finesses that are due to these factors are referred to as the reflectivity finesse, F_R, the flatness finesse, F_F, and the aperture finesse, F_A. The first two can be combined,[4] $\left(\frac{1}{F_I^2} = \frac{1}{F_R^2} + \frac{1}{F_F^2}\right)$, where F_I is the instrument finesse. The third becomes important if the aperture diameter is large. These three factors can then be combined as

$$\frac{1}{F_S^2} = \frac{1}{F_A^2} + \frac{1}{F_R^2} + \frac{1}{F_A^2},$$

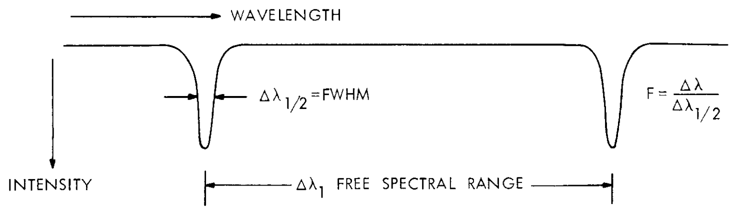

Fig. VIII-31. Definition of finesse.

where F_S is the over-all system finesse.

a. Instrument Finesse

The reflectivity finesse is given by $F_R = \pi\sqrt{R}/1-R$. For our case (R = 0.97), F_R is calculated to be ~100.

The flatness finesse is given by $F_F = a/2$, where a is the flatness factor of the plates. For the plates used in this interferometer (flat to $\lambda/100$, a = 100), $F_F = 50$.

From these values, the instrument finesse, F_I, is calculated to be 44.5. This was also measured using a coherent He-N2 laser radiation at $\lambda = 6328$ Å with d = 0.1 mm. At this value of d, $\Delta\lambda = 20$ Å. The FWHM of the 6328 Å laser radiation is $10^{-3} - 10^{-4}$ Å. Therefore, the observed value of $\Delta\lambda_{1/2}$ is solely due to the instrument broadening. From this measurement, $F_I = 39$ is obtained. In the subsequent calculations this value of the instrument broadening is used.

b. Aperture Finesse

The divergence angle, ϕ, of the rays collimated by lens L_2 in Fig. VIII-30 depends on the aperture diameter, A(θ A/f, where f is the focal length of the lens L_2). A monochromatic line will, therefore, appear broadened to $\Delta\lambda_A$ because of the diverging rays, where $\delta\lambda_A = \lambda\theta^2/8$. Using the relationships $\theta = A/f$, $F_A = \Delta\lambda/\delta\lambda_A$, and $\Delta\lambda = \lambda^2/2d$, we obtain $F_A = 4\lambda f^2/dA^2$. Note that F_A is inversely proportional to A^2.

c. Over-all "System" Finesse

F_A was calculated for f = 126 mm and $\lambda = 6328$ Å. In Fig. VIII-32 the over-all system finesse, F_S, is shown as a function of d for various values of A. At small values of d, F_S is limited by the instrument finesse which is constant for a given set of plates, while at large values of d, the aperture finesse is the limiting factor.

An experiment was performed to check the accuracy of these calculations for the optical system that was used to observe the radiation emitted by the plasma. A noncoherent diffused laser beam was used for this purpose. A diverging lens was put in between lens L_1 and the aperture. The lens was tilted so that the aperture was illuminated by the outer regions of the divergent laser beam rather than the central portion.

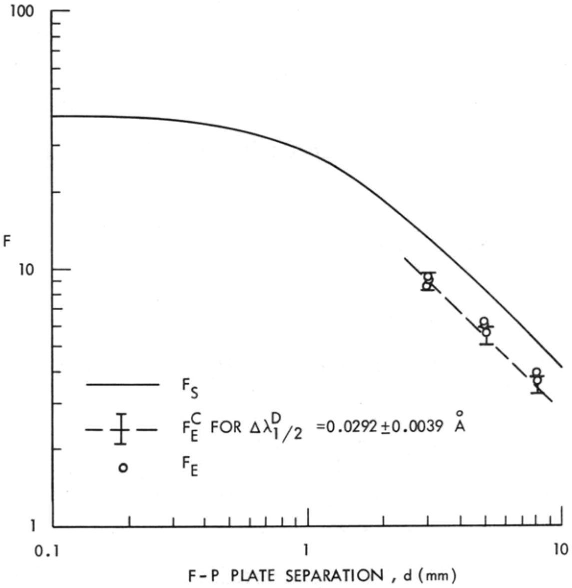

Fig. VIII-32. Finesse vs d for λ = 6328 Å, f = 126 mm.

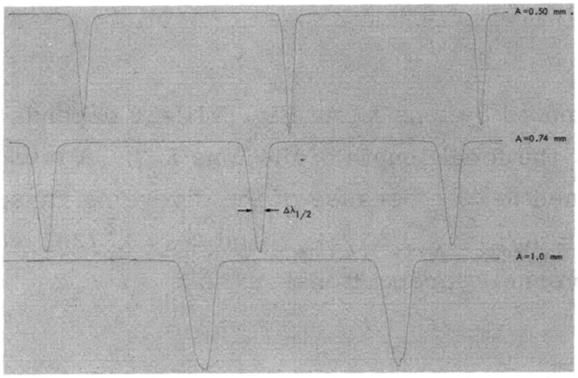

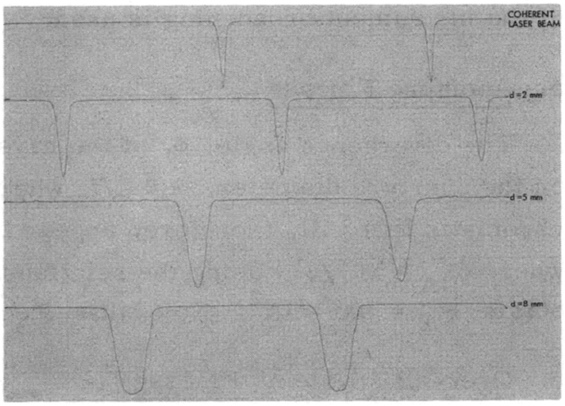

Fig. VIII-33.

Scans of diffused noncoherent laser beam (λ = 6328 Å) for d = 5 mm and variable A.

Fig. VIII-34.

Scans of diffused noncoherent laser beam (λ = 6328 Å) for A = 0.84 mm and variable d.

Furthermore, a few layers of mylar were put before the aperture to diffuse the laser radiation and to destroy its coherence. In Figs. VIII-33 and VIII-34 typical scans of the diffused noncoherent laser radiation are shown for constant d and variable A; and for constant A and variable d, respectively. Since the natural width of the 6328 Å laser radiation is negligible, the observed variation in $\Delta\lambda_{1/2}$ is due to the system finesse shown in Fig. VIII-32. In this figure, the measured values of finesse, F_E, obtained from a collection of such data, were also shown. The agreement between the calculated, F_S, and the measured, F_E, values is reasonably good. The same measurements were repeated using a naturally noncoherent light source (5461 Å radiation of a Mercury Geissler tube, which at room temperature has a Doppler broadening of ~0.005 Å), and similar agreement between F_S and F_E was obtained. These measurements, thus show that the over-all system finesse of the optical system, including the aperture effect, can be predicted within an accuracy of a few per cent.

These results should apply, without modification, to a system in which the rays incident on the Fabry-Perot plates may have large divergence (for example, when the collimating lens L_2 is removed). In this case a lens would be put in following the interferometer to focus the fringes, and the aperture A at the focal point of this lens would be used to observe the intensity of the central fringe only.

Measurement of the Broadening of A II 4610 Å Radiation from the ECR Plasma

System finesse values were also calculated for $\lambda = 4610$ Å, for A = 0.50, 0.64, 0.74 and 0.84 mm. Plots of F_S against d are shown in Figs. VIII-35 and VIII-36.

With the system just described, scans of A II 4610 Å were taken for various values of d and A. Typical data are shown in Figs. VIII-37 for d = 3 mm and A = 0.5 mm. Experimental values of finesse, F_E, were obtained from such data by taking the ratio of $\Delta\lambda$ to $\Delta\lambda_{1/2}$. The values of F_E, shown also in Figs. VIII-35 and VIII-36, are considerably lower than F_S for $\lambda = 4610$ Å. This indicates that the 4610 Å line radiation from the plasma has a significant amount of broadening compared with the system broadening. From the observed values of $\Delta\lambda_{1/2}$, the true broadening of the 4610 Å line, $\Delta\lambda^D_{1/2}$, was obtained by using the relationship

$$\Delta\lambda^D_{1/2} = \sqrt{(\Delta\lambda_{1/2})^2 - (\delta_S)^2},$$

where $\delta_S = \Delta\lambda/F_S$. This is the convolution mainly of the aperture function and the Gaussian true line profile. Using the data for these four values of A and $1.5 \leq d \leq 8$ mm, a value of $\Delta\lambda^D_{1/2} = 0.0292 \pm .0039$ Å was obtained which represents ~13% variance.

The expression $\Delta\lambda^D_{1/2} = \sqrt{(\Delta\lambda_{1/2})^2 - (\delta_S)^2}$ is a first-order approximation out for

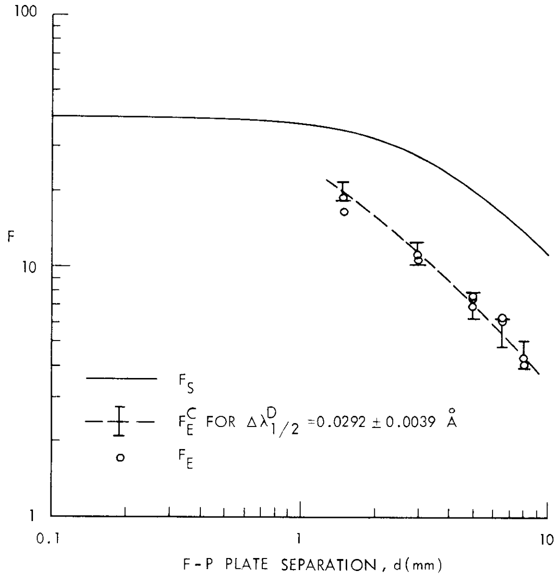

Fig. VIII-35. Finesse vs d for λ = 4610 Å, f = 126 mm, A = 0.50 mm.

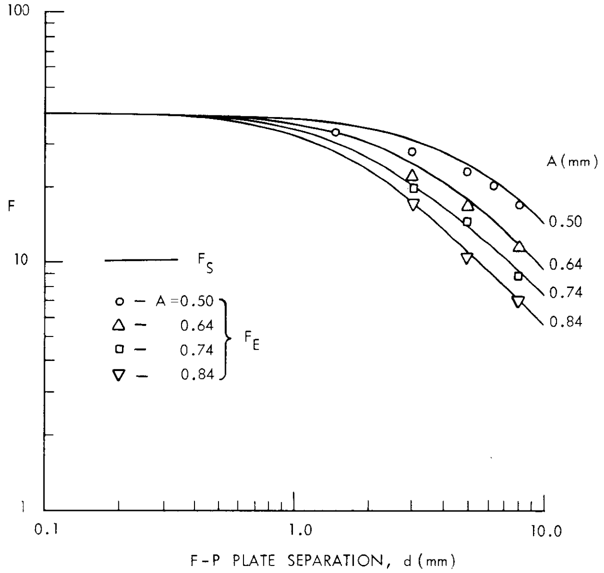

Fig. VIII-36. Finesse vs d for Y = 4610 Å, f = 126 mm, A = 0.84 mm.

a Gaussian line (with $\Delta\lambda^{D}_{1/2}$ = FWHM) and a square aperture function (width = δA). The fit of the relationship $\Delta\lambda^{D}_{1/2} = \sqrt[3]{(\Delta\lambda_{1/2})^{2} - \delta_{A}^{2}}$ (where $\Delta\lambda_{1/2}$ is the FWHM of the convoluted profile) to the results obtained graphically represents an error of approximately 12%, while that of the relationship $\Delta\lambda^{D}_{1/2} = \sqrt{(\Delta\lambda_{1/2})^{3} - \delta_{A}^{3}}$ is ~2.5%. This convolution accounts, however, only for the aperture effect, and not the instrument broadening. More detailed unfolding of the actual line broadening will be carried out in the near future.

The description of the plasma was reported in a previous report[1] and further study of the plasma appears in this issue (see Sec. VIII-B. 2). Here we shall mention briefly that for these measurements the following parameters were used: microwave power, 50 W; drift field, 0.8 kG; and neutral pressure, 2×10^{-5} Torr.

Under these running conditions, $n_e \approx 2\text{-}5 \times 10^{10}$ and $T_e \approx 5\text{-}10$ eV. The radiation observed in these measurements is emitted from a small volume in the center of the plasma column (determined by the aperture) near the source region. The observations were made perpendicular to the B-field.

No final conclusion has been reached on the factors contributing to the true line broadening of $\Delta\lambda^{D}_{1/2} = 0.0292 \pm .0039$ Å. The factors that should be considered are Zeeman splitting, rotation of the plasma, and thermal motion of ions. If indeed the thermal motion of ions is the dominant factor, these results would indicate that ion temperature is approximately 0.27 ± .06 eV.

Observation of Multiple Modes in the He-Ne Laser Radiation at λ = 6328 Å

During this study, we also checked the capability of the interferometer. In Fig. VIII-37 we show a scan of the coherent He-Ne laser radiation at 6328 Å radiation with d = 15 mm. What we observe here is 3 modes separated by ~0.007 Å. This value agrees well with that expected for the laser which has an optical cavity length of approximately 30 cm.

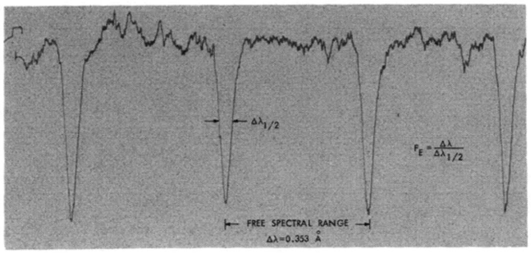

Fig. VIII-37.
Scan of A II 4610 Å line emitted by the ECR heated plasma (d = 3 mm, A = 0.5 mm).

Conclusions

This study shows that it is possible (i) to measure the over-all system finesse of a Fabry-Perot interferometer by using a noncoherent diffused laser beam; and (ii) to measure broadening of lines emitted by low intensity steady-state plasmas by using sufficiently large aperture and then taking into account the contributions of aperture to the observed broadening. Using this method, we shall measure braodening of the A II 4610 Å lines in the ECR plasma under various experimental conditions. We hope that interpretation of these measurements will shed some light on the energetics and the properties of the plasma.

E. Oktay, J. T. Reed III, L. M. Lidsky

References

1. J. E. Robinson, E. Oktay, L. M. Lidsky, and R. A. Blanken, Quarterly Progress Report No. 97, Research Laboratory of Electronics, M. I. T., April 15, 1970, pp. 92-101.
2. J. K. Silk, Ph. D. Thesis, Department of Physics, M. I. T., August 1969.
3. M. Hudis, S. M. Thesis, Department of Nuclear Engineering, M. I. T., June 1967.
4. J. R. Greig and J. Looper, Appl. Opt. 7, 2166 (1966).

VIII. APPLIED PLASMA RESEARCH[*]

C. Plasma Effects in Solids

Academic and Research Staff

Prof. A. Bers
Dr. L. D. Pleasance

Graduate Students

J. H. Cafarrella
C. M. Krowne

1. EXCITATION OF SURFACE WAVES ON SEMICONDUCTORS

The dispersion characteristics of electron surface waves have been described in previous reports.[1, 2] In this report the excitation of electron surface waves by electrodes placed on or near the surface will be examined. Comparison with the excitation of surface acoustic waves on piezoelectric materials will be made.

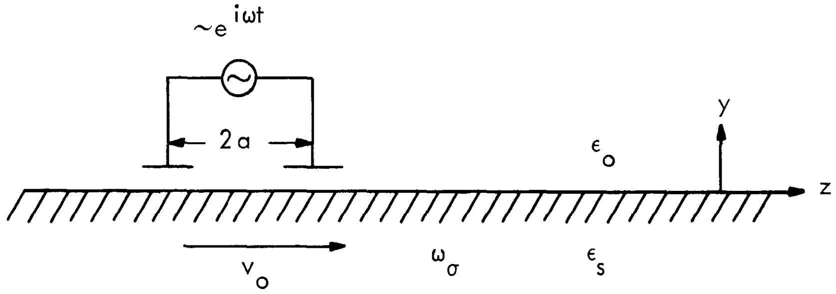

Fig. VIII-38. Geometry for excitation of electron surface waves.

The geometry under consideration is shown in Fig. VIII-38. Electrons with a dielectric relaxation frequency ω_σ fill a semiconductor for $y \leqslant 0$. The dielectric coefficient of the lattice is ϵ_s and that of the space above is ϵ_o. The electrons when drifting parallel to the surface will support a quasi-static surface wave that propagates in the direction of the drift with a group velocity close to v_o. This wave is driven by a pair of thin metallic electrodes placed on or near the surface. A solution of the electrical problem which relates the impedance of the driven electrodes to the amplitude of the electron surface wave is required.

The charge distribution on the electrodes will be approximated by a surface

---

[*] This work was supported by the National Science Foundation (Grant GK-18185), and in part by M.I.T. Lincoln Laboratory Purchase Order No. CC-554.

charge distribution of the form

$$\rho_s^* = \rho_o \sin(q_o z), \quad -2a \leqslant z \leqslant 2a$$
$$= 0, \quad z < -2a,\ z > 2a, \tag{1}$$

where $k_o = \pi/2a$, and 2a is the center-to-center electrode spacing. This distribution may be considered as the first term of the Fourier series for the detailed charge distribution.

The equations governing the system are

$$\nabla \cdot \overline{D} = \rho_e + \rho_s^* \tag{2}$$

$$\nabla \cdot \overline{J} + \frac{\partial \rho_e}{\partial t} = 0 \tag{3}$$

$$\overline{J} = \omega_\sigma \epsilon_s \overline{E} + \overline{v}_o \cdot \nabla \rho_e, \tag{4}$$

where $\overline{D} = \epsilon \overline{E}$, and $\overline{E} = -\nabla \phi$. The effects of electron diffusion and of a static magnetic field may be included by the addition of appropriate terms in Eq. 4. The boundary condition at $y = 0$ is the continuity of the normal component of $\overline{D}$:

$$D_y(y=0+) - D_y(y=0-) = \rho_s^* + \rho_e^*. \tag{5}$$

A Fourier transformation, $e^{i(\omega t+qz)}$, followed by a Laplace transformation, e^{py}, applied to Eqs. 1-5 gives

$$p\left(\epsilon_s + \frac{i\omega_\sigma \epsilon_s}{\omega - qv_o} + \epsilon_o\right)\phi(q) = \rho_s^*(q), \tag{6}$$

where

$$\rho_s^*(q) = \rho_o \frac{\sin 2(q+q_o)a}{q+q_o} - \rho_o \frac{\sin 2(q-q_o)a}{q-q_o} \tag{7}$$

is the Fourier transform of ρ_s^*, and $p = \pm q$. The sign of p is so chosen that the fields vanish at $y = \pm\infty$. For $\rho_s^* \equiv 0$, Eq. 6 defines the dispersion relation for surface waves on a cold electron plasma:

$$qv_o - \omega - iM\omega_\sigma = 0, \tag{8}$$

where

$$M = \frac{\epsilon_s}{\epsilon_s + \epsilon_o}.$$

The potential at the surface is obtained by a Fourier inversion of Eq. 6:

$$\phi(z) = \frac{-i\rho_o}{2\pi(\epsilon_o+\epsilon_s)} \int_{-\infty}^{\infty} dq \, \frac{e^{-iqz}}{p} \, \frac{\sin 2(q-q_o)a}{q - q_o} \, \frac{q - q_d}{q - q_e}, \tag{9}$$

where $q_d = \omega/v_o$, and $q_e = \left(1 + iM \frac{\omega_\sigma}{\omega}\right) q_d$. Only the second term in Eq. 7, which corresponds to excitation of waves in the direction of v_o, will be considered.

The integral in Eq. 8 may be solved by contour integration in the complex q-plane along the path shown in Fig. VIII-39. There are four contributions to the integral: (i) from a pole at q_e corresponding to wave excitation, (ii) from a pole at q_o corresponding to local fields under the electrodes, (iii) from a pole at $q = 0$ corresponding to a constant electrostatic potential, and (iv) from a branch cut corresponding to end effects of the electrodes. The last two contributions can be evaluated separately, and will be neglected. An additional feature of Eq. 8 is the zero at q_d. The relative position of the pole at q_e and the zero at q_d determine the character of the impedance variation as the drift velocity is changed.

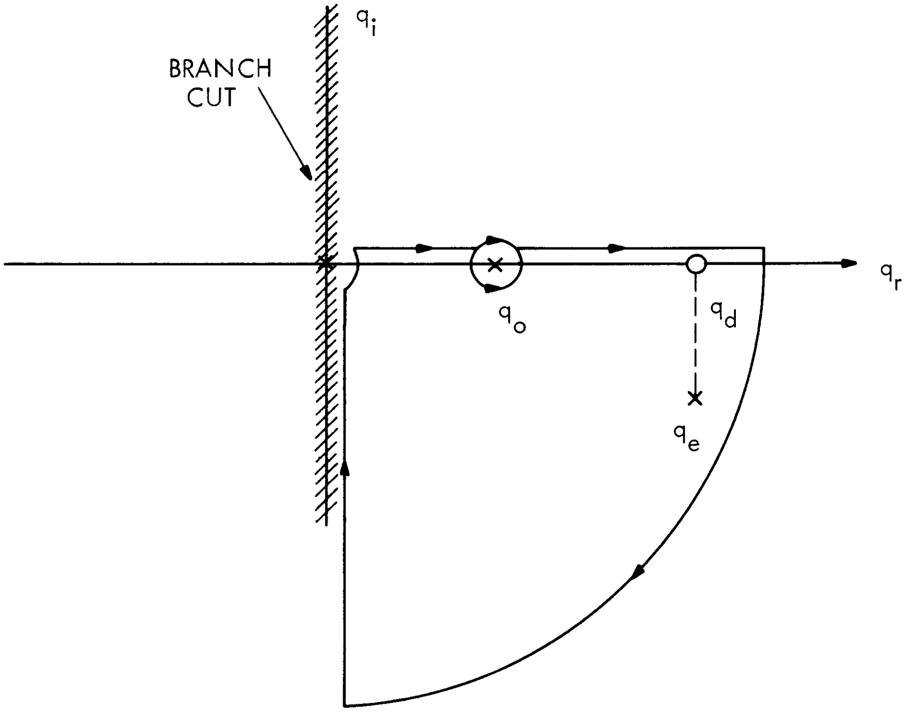

Fig. VIII-39. Typical integration contour in the q-plane.

From the contributions to the integral at points under the electrodes, the potential difference between points z = ±a is found to be

$$\Delta\phi = \frac{-\rho_o}{\epsilon_o + \epsilon_s}\left[\frac{\sin q_o a}{q_o}\,\frac{(q_o - q_d)}{(q_o - q_e)} + \frac{\sin q_e a}{q_e}\,\frac{q_e - q_d}{q_e - q_o}\, e^{-2i(q_e - q_o)a}\right] e^{-iq_o a}. \tag{10}$$

Equation 10 defines a relative surface impedance:

$$Z\omega C_o = -i\,\frac{q_o - q_d}{q_e - q_o} + i\,\frac{q_e - q_d}{q_e - q_o}\,\frac{q_o}{q_e}\, e^{-2iq_e a} \sin q_e a, \tag{11}$$

where $C_o = q_o(\epsilon_s + \epsilon_o)$ is the capacitance per unit area in the absence of electrons. The first term of Eq. 11 represents the contribution from local fields of the electrodes (in the absence of end effects), and is just that expected for a unit cell of a periodic charge distribution. The second term represents the contribution to the impedance of the excitation of surface waves.

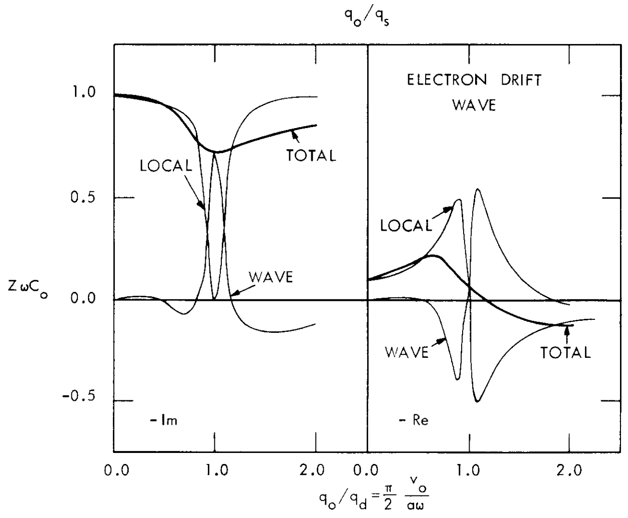

Fig. VIII-40. Terminal impedance variation for the excitation of electron surface waves.

The variation of the impedance with increasing drift velocity is shown in Fig. VIII-40. The separate contributions from each term and their sum are shown. The parameter $\frac{\delta q}{q} = \frac{q_e - q_d}{q_d}$ is the relative separation between the pole and zero in Eq. 9 associated with wave propagation. The curves in Fig. VIII-40 correspond to a weakly damped electron drift wave with $M\,\frac{\omega_\sigma}{\omega} = 0.1$.

The resistive part of the impedance can be seen to be negative for $q_o/q_d \gtrsim 1$, and the drifting electrons may be used as an active medium to drive other modes of the system. The generation of waves contributes an inductive term to the reactance.

It is interesting to compare the excitation of electron drift waves that display the characteristics of an active medium with the excitation of the more familiar acoustic wave in the absence of electrons. The dielectric coefficient of a medium which will support a surface acoustic wave may be expressed as

$$\epsilon_p = \epsilon_s + K^2 \epsilon_s \frac{q_s}{q - q_s}, \tag{12}$$

where $q_s = \omega/v_s$ is the wave number of the acoustic wave in the absence of piezoelectricity, and K^2 is the effective electromechanical coupling constant. By following the same procedure as for the drift wave similar expressions will be generated for the impedance (Eq. 11) with the zero at q_d replaced by q_s and the pole at q_e replaced by $q_a = (1-MK^2)q_s$, as shown in Fig. VIII-41. The primary difference in the excitation of the two waves is that $\delta q/q = -MK^2$ is real for the acoustic wave, while $\delta q/q = -IM \frac{\omega_\sigma}{\omega}$ is pure imaginary for the electron wave. The impedance variation for the acoustic wave is shown in Fig. VIII-42 for $\delta q/q = -0.1$. This value is used to facilitate comparison with Fig. VIII-40. The resistive component of the impedance of the acoustic system is now positive-definite as expected. The similarity in the variation of the components of Fig. VIII-40 and Fig. VIII-42 is apparent and reflects the change in phase of $\delta q/q$.

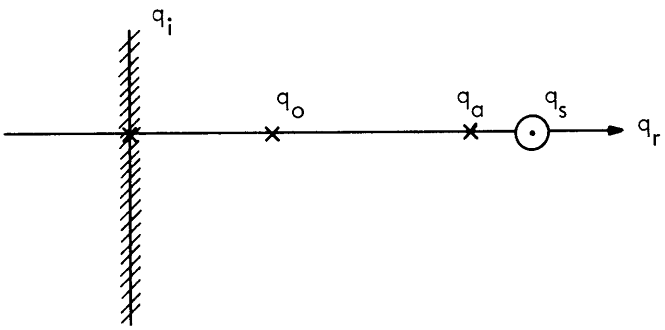

Fig. VIII-41. Position of the poles and zeros of the acoustic wave on the q-plane.

From this discussion it is clear that the parameter $M \frac{\omega_\sigma}{\omega}$ plays the role of a coupling constant in the excitation of electron drift waves. Many of the

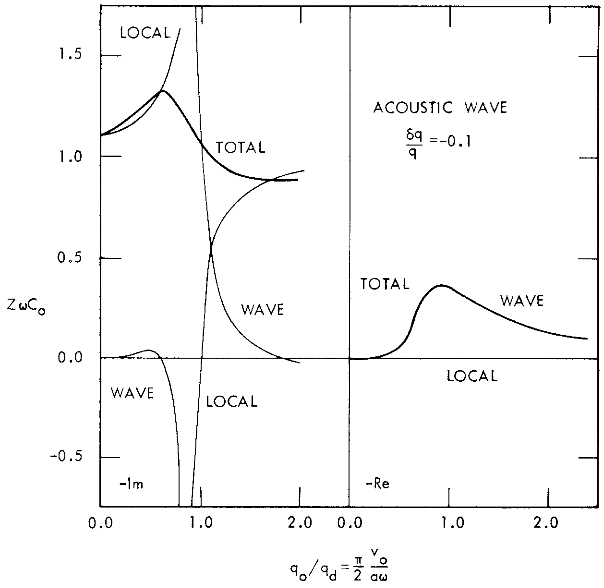

Fig. VIII-42. Terminal impedance variation for the excitation of acoustic waves.

basic features of the excitation of these waves may be deduced from the more familiar acoustic-wave excitation.

L. D. Pleasance

References

1. A. Bers, Quarterly Progress Report No. 99, Research Laboratory of Electronics, M.I.T., October 15, 1970, p. 96.
2. L. D. Pleasance and A. Bers, Quarterly Progress Report No. 99, Research Laboratory of Electronics, M.I.T., October 15, 1970, p. 101.

2. SMALL-SIGNAL CONSERVATION THEOREM FOR THE ELECTRON PLASMA SURFACE WAVE ON A SEMICONDUCTOR

In previous reports[1, 2] we derived the dispersion characteristics of electron plasma surface waves in crossed electric and magnetic fields. Under conditions for which these waves are weakly damped, we found that the time-averaged small-signal energy, as derived from the dielectric function for the medium, could be either positive or negative, depending upon the direction of the applied magnetic field relative to the applied electric field. In this report we present a small-signal conservation theorem which further elucidates the physical nature of the energy and energy flow.

For simplicity, we shall ignore the effects of diffusion. The small-signal equations for the electrons and quasi-electrostatic fields are then[1]

$$\nu m\bar{v}_1 = e(\bar{E}_1+\bar{v}_1\times\bar{B}_o) \qquad (1)$$

$$\epsilon \frac{\partial \overline{E}_1}{\partial t} + e\overline{\Gamma}_1 = 0, \tag{2}$$

where $\overline{\Gamma}_1$ is the first-order particle current density. For the mode of interest we assume that electron bunching occurs only at the surface of the semiconductor (see Fig. VIII-43), so that

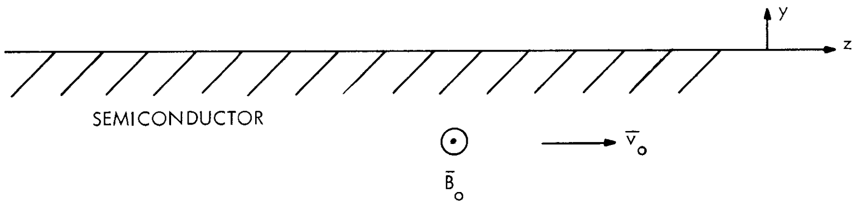

Fig. VIII-43. Semiconductor surface.

$$\overline{\Gamma}_1 = n_o\overline{v}_1 + n_{1s}\delta(y)\,\overline{v}_o, \tag{3}$$

where

$$n_{1s} = n_o\xi \tag{4}$$

and

$$v_{1y} = \frac{d\xi}{dt} = \frac{\partial \xi}{\partial t} + v_o\,\frac{\partial \xi}{\partial z}. \tag{5}$$

Dot-multiplying Eq. 2 by $\overline{E}_1$ and using Eqs. 1, 3, 4, and 5, we find

$$\frac{\partial}{\partial z}\,s_M + \frac{\partial}{\partial t}\,(w_e + w_M) + p_d = 0, \tag{6}$$

where

$$s_M = (1/2)\;en_o\xi\delta(y)\;\overline{v}_o \times \overline{B}_o \cdot \overline{\xi}v_o \tag{7}$$

$$w_e = (1/2)\;\epsilon E_1^2 \tag{8}$$

$$w_M = (1/2)\;en_o\xi\delta(y)\;\overline{v}_o \times \overline{B}_o \cdot \overline{\xi} \tag{9}$$

$$p_d = \nu m n_o\left[v_1^2 + \xi\delta(y)\overline{v}_o \cdot \overline{v}_1\right]. \tag{10}$$

Equation 6, when integrated over y, is the desired conservation theorem.

Equation 9 has a simple physical interpretation for the energy density associated with the small-signal motion of the electrons: It is the work done in establishing the small-signal displacement ξ perpendicular to the surface. The sign of w_M depends only upon the sign of $e\bar{v}_o \times \bar{B}_o$. We note, also, that the small-signal power dissipated, Eq. 10, may also be negative. When the power dissipated is negligible compared with the energy flow, weakly damped waves exist, and those having negative energy can be used to extract energy from the electrons. In the opposite limit energy may be extracted from the electrons if the power dissipated is negative. The first possibility can lead to resonant amplification of signals,[3] while the latter contributes to nonresonant amplification.

A. Bers

References

1. A. Bers, Quarterly Progress Report No. 99, Research Laboratory of Electronics, M.I.T., October 15, 1970, pp. 96-100.
2. L. D. Pleasance and A. Bers, Quarterly Progress Report No. 99, Research Laboratory of Electronics, M.I.T., October 15, 1970, pp. 101-105.
3. A. Bers and B. F. Burke, Appl. Phys. Letters 16, 300 (1970); 17, 47 (1970).